Journal of the Earth Simulator, Volume 1, April 2004, 35–56

A Fifty-Year Eddy-Resolving Simulation of the World Ocean – Preliminary Outcomes of OFES (OGCM for the Earth Simulator) –

Yukio Masumoto[1]*, Hideharu Sasaki[2], Takashi Kagimoto[1], Nobumasa Komori[2], Akio Ishida[1], Yoshikazu Sasai[1], Toru Miyama[1], Tatsuo Motoi[1], Humio Mitsudera[3+], Keiko Takahashi[2], Hirofumi Sakuma[2] and Toshio Yamagata[1]

[1] *Frontier Research System for Global Change, Yokohama, Kanagawa, Japan*
[2] *The Earth Simulator Center, Yokohama, Kanagawa, Japan*
[3] *International Pacific Research Center, Honolulu, Hawaii*
+ Now at Institute of Low Temperature Science, Hokkaido University

(Received February 9, 2004; Revised manuscript accepted April 26, 2004)

Abstract A fifty-year eddy-resolving simulation of the world ocean has been performed on the Earth Simulator for the first time. Several global aspects of the circulations and regional characteristics in some specific areas simulated in the high-resolution model are compared to available observations. The results demonstrate a promising capability of representing realistically meso-scale variability, including separation of the western boundary current from the coast, meso-scale eddy generation near the strong current systems, as well as appropriate water masses in the world ocean. This climatological simulation was finished within one month of the wall-clock time, suggesting a possibility of a quite long-term eddy-resolving simulation and/or a large number of case studies and parameter studies. This success encourages further advance toward a super-high resolution coupled simulation of the atmosphere and the ocean.

Keywords: High-resolution ocean general circulation model, high performance parallel computing, climatological ocean circulation, meso-scale eddy

1. Introduction

Ocean general circulation models (OGCMs) have long been utilized for studies on ocean circulations, climate systems, and their variations with various spatial and temporal scales. During the early stage of the OGCM simulations, the appreciation on the usefulness of the models compared with traditional scientific methodologies of observations and theoretical considerations was relatively low. It took time for the community to realize that the model solutions can skillfully reproduce the observed features of the world oceans. In recent years, owing to the advances in the physics and numerical schemes of the OGCM itself and in the computational power and techniques, overall features of large-scale ocean circulations are well reproduced under appropriate boundary conditions even in the models with moderate grid spacing, which cannot take into account direct effects of meso-scale eddies and other small-scale contributions.

However, a few pilot studies initiated in 1990s on higher resolution simulations covering either the basins of interest or near global domain showed a promising capability of our state of the art OGCMs to reproduce not only basin-scale phenomena but also the meso-scale activities embedded in the background large-scale circulations, including proper positioning of the energetic western boundary currents. So far, there are several, but limited number of attempts to build such an eddy-resolving global or basin-scale OGCM. Pioneering work of Semtner and Chervin [1] would be the first one aiming at the impact study of an eddy permitting simulation on the global domain. Fine Resolution Antarctic Model (FRAM) is another example designed for the study on the effects of the small-scale phenomena on the Antarctic Circumpolar Current (ACC) [e.g. 2, 3]. Recently, an eddy-resolving model with the horizontal grid spacing of 1/10° for the North Atlantic Ocean is developed under the World Ocean Circulation Experiment (WOCE) project [4]. The results from this basin-scale model indicate that, to reproduce quantitatively the root-mean-square variance of the sea surface height anomaly in the North Atlantic Ocean, the model should have the horizontal grid spacing of the

* ***Corresponding author***: *Yukio Masumoto, Climate Variations Research Program, Frontier Research System for Global Change, 3173–25 Showa-Machi, Kanazawa, Yokohama, Kanagawa, 236-0001 Japan. E-mail: masumoto@jamstec.go.jp*

order of 1/10° or finer. Following these attempts of the high resolution simulations of the ocean, the high-resolution global models with the horizontal grid spacing of 1/12° and 1/10° are being developed in Southampton Oceanography Center as an extension of the OCCAM [5] and in Los Alamos National Laboratory for the Parallel Ocean Program (POP), respectively.

It is, however, quite time-consuming work for the high resolution simulation to integrate long enough for the study on the seasonal to interannual variability of the ocean circulations, since the computer power and resources available for our community are not yet sufficient. Reflecting the recent growing and compelling concerns for the global climate simulation studies as well as the high-resolution simulations, the construction of the Earth Simulator (hereafter, referred to ES) was initiated in 1997 with a distinguished leadership of late Dr. Miyoshi[1]. He set a goal of developing an efficient multi-purpose parallel hardware system that outperforms the contemporary super-computers in a commercial base both in the capacity of the main memory and sustained computational performance by a factor of one thousand. With the advent of the ES, the long-term eddy-resolving simulation becomes feasible to investigate details of the fine structure of the ocean currents and influence of the eddies on the larger circulations.

As the first step toward a full global eddy-resolving OGCM for the study on the climate variability, we started off with constructing a high-resolution OGCM that focuses on the circulation in the low and mid latitude regions. The model is based on the one used widely in the community, but tremendous efforts were put for the efficient parallelization for the ES. The model with the horizontal grid spacing of 1/10° can be run on the ES for 50 model years within a month of the wall-clock time, and this makes it possible to perform a quite long integration or a series of sensitivity studies with different parameters, parameterizations, and boundary conditions with the eddy-resolving resolution. At this initial stage, our attempts are rather straightforward in terms of the model configuration, numerical schemes, and the parameterization of the unresolved physics in the model. However, we expect to have useful informations from the model outputs for better understanding of the ocean circulations and their variability and for improving the OGCM further.

In this article, we highlight several interesting features simulated in a fifty-year integration of the high-resolution model, together with the description of the model. In section 2, both model configuration and parallelization procedure are described. Global aspects of the simulated results are shown in section 3, while details of the simulated circulations in several key regions are indicated in section 4. Section 5 summarizes the results and discusses future direction of the high-resolution simulation with specific issues found in this preliminary fifty-year run.

2. OGCM for the Earth Simulator (OFES)

Our high-resolution ocean model for the ES (hereafter referred to OFES) is based on the Modular Ocean Model (MOM3) [6], developed at Geophysical Fluid Dynamics Laboratory/National Oceanic and Atmospheric Administration (GFDL/NOAA), with the significant modifications on the parallelization procedures. The computational domain covers a near-global region extending from 75°S to 75°N except for the Arctic Ocean (Fig. 1), with horizontal grid spacing of 1/10°. There are 54 vertical levels, with varying distance between the levels from 5 m at the surface to 330 m at the maximum depth of 6,065 m. The distribution of the vertical levels is determined so as to reproduce realistic ocean circulations above the main thermocline. The model topography is constructed from the 1/30° bathymetry dataset created by the OCCAM project at the Southampton Oceanography Centre (obtained through GFDL/NOAA). The partial cell method included in MOM3 allows us to fit the bottom topography into the model as realistic as possible.

A scale-selective damping of bi-harmonic operator is adopted for horizontal mixing of the momentum and tracers, to suppress computational noises with the horizontal scale of the grid spacing. The viscosity and diffusivity vary in space, with the coefficients proportional to the cube of the zonal distance between the grids [4]. The background horizontal bi-harmonic viscosity and diffusivity are -27×10^9 m^4s^{-1} and -9×10^9 m^4s^{-1}, respectively. For the vertical mixing, the KPP boundary layer mixing scheme [7] is employed.

Monthly mean wind stresses averaged from 1950 to 1999 from the NCEP/NCAR reanalysis data are used for the climatological seasonal integration. The surface heat flux is calculated by the same bulk formula with Rosati and Miyakoda [8], using the monthly mean values from the NCEP/NCAR reanalysis outputs for the necessary datasets. Also, the precipitation rate from the same reanalysis date is utilized to obtain the fresh water flux. In addition to this fresh water flux, we adopted additional restoring to the monthly mean sea surface salinity of the World Ocean Atlas 1998 (henceforth WOA98) [9, 10, 11], with the restoring time-scale of 6 days to include the contribution from the river run-off. In the buffer zones within 3° latitu-

[1] *Dr. Miyoshi deceased on November 2001, just three months before the Earth Simulator has fully implemented for test operations. He was a first director of Earth Simulator Research and Development Center.*

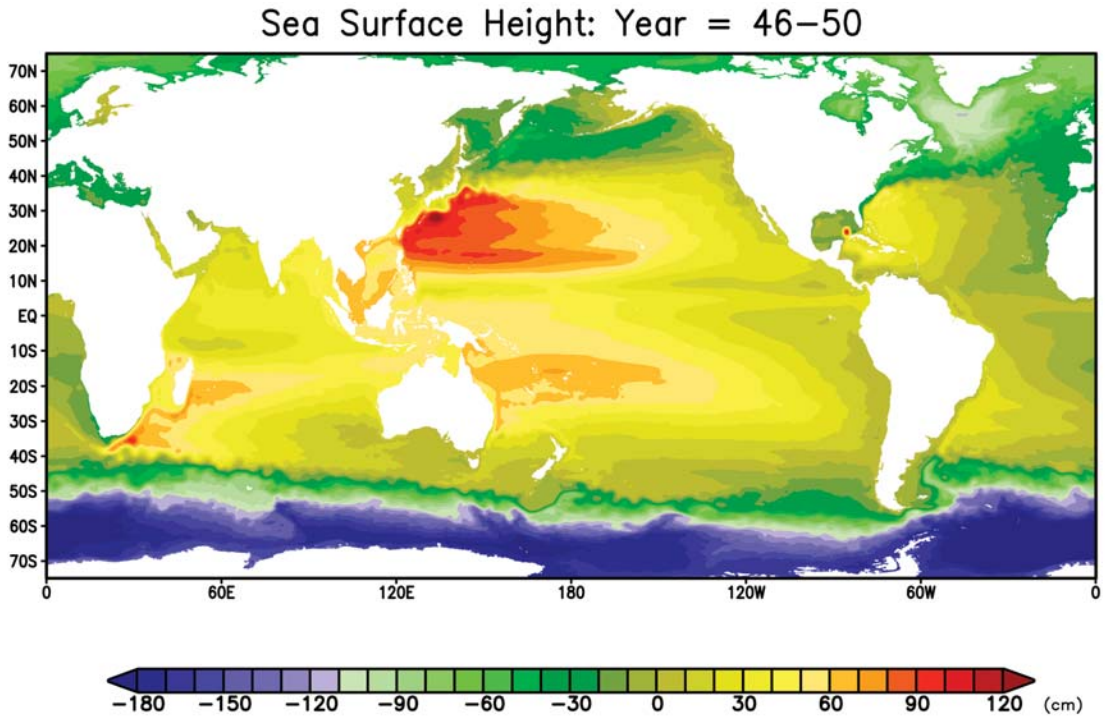

Fig. 1 Five-year mean distribution of sea surface height [cm] from year 46 to 50 for the whole domain of the model.

Table 1 Routine-wise vector length, ratio and the total flops elapsed.

Main computation [routine names]	CPU time (%)	MFLOPS	Vector Ratio	Ave. Vector Length
baroclinic computation [baroclinic]	14.3	4900.7	99.8	240.0
vertical mixing with implicitly [invtri]	13.0	3374.6	99.6	240.0
barotropic coputation [expl_freesurf]	11.0	4902.6	99.7	240.0
unesco_density [unesco_density]	8.4	5202.2	99.8	256.0
computation with biharmonic [delseq_velocity]	7.5	4255.7	99.7	240.0
main computation of tracers [tracer]	7.1	5025.9	99.8	240.0
calculate advection velocities [adv_vel]	4.2	4838.7	99.6	240.0
construct diagnostics [diagt1]	2.6	3801.6	99.5	243.0
computation of normalized densities [statec]	2.4	6613.0	99.8	240.1

dinal distances near the northern and southern artificial boundaries, the temperature and salinity fields are restored to the monthly mean climatological values (WOA98) at all depths [12, 13, 14, 9, 10, 11]. The restoring time-scale at those boundaries is set to be 1 day and it increases linearly to the infinity in the interior region. The model is integrated for 50 years from the annual mean temperature and salinity fields (WOA98) without motion.

3. Code optimization and computational performance

To attain the best performance of our model code, a number of different optimization techniques have been utilized, considering distinctive characteristics of the ES. First of all, each routine must be optimally vectorized to improve the performance on vector machines as the ES. In addition, we applied such common techniques as inline expansions, loop collapse, loop unrolling/rerolling together with re-ordering in order to reduce the number of calling procedures and to make the averaged length of do-loops longer. In some cases, techniques of loop fission/splitting and loop fusion are reintroduced in a balanced manner.

As the first step of the optimization, we attempted to make the vector ratio of almost all routines to exceed

Table 2 Scaling factor with 4 halo regions.

Total CPU		12	20	60	100	300	500	1500
MPI	lines /CPU	129	79	29	19	9	7	5
	scaling factor	11.63	18.99	51.72	78.95	166.67	214.29	300.00
MPI + autotasking*	lines /CPU	126	76	26	16	6	4	2
	scaling factor	11.90	19.74	57.69	93.75	250.00	375.00	750.00

* 4 parallelized for intra-node

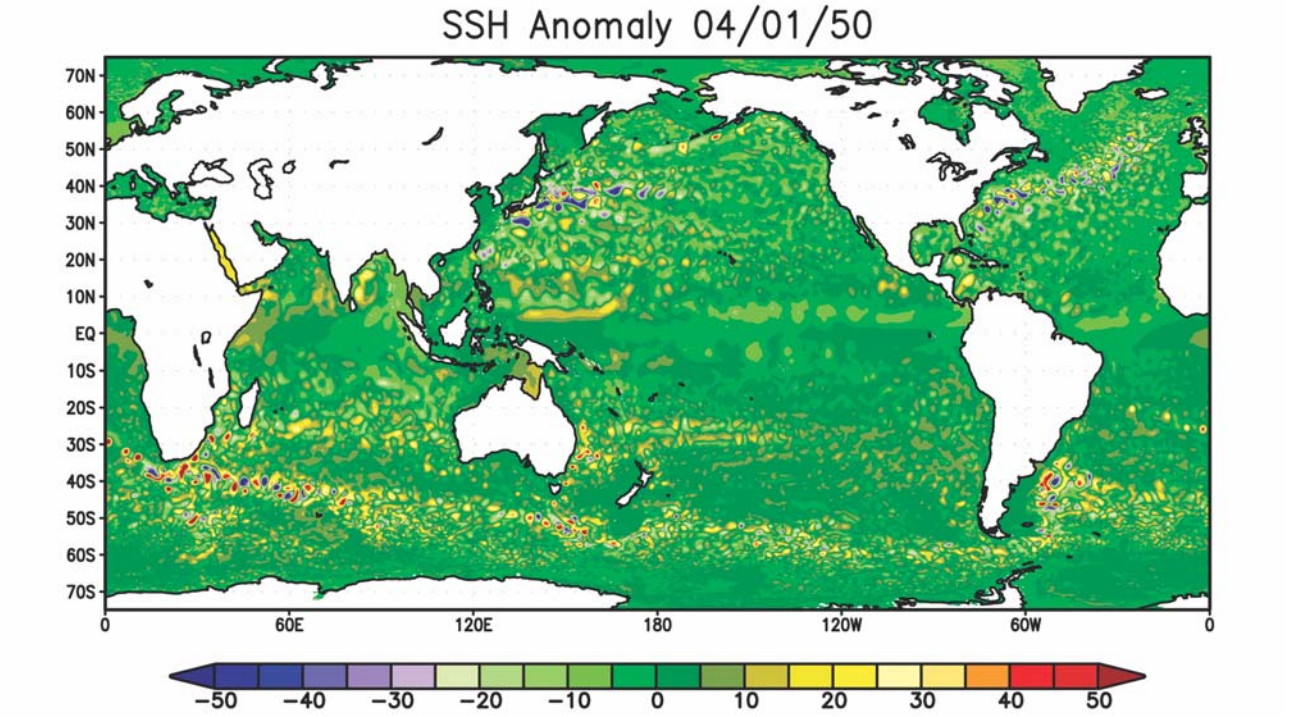

Fig. 2 Snapshot of the sea surface height anomaly at April 1 of Year 50. The anomaly is calculated relative to the five-year mean sea surface height shown in Fig. 1.

99.5%. Values of averaged vector length, vector ratio and the total flops for the several routines after the optimal tuning are indicated in Table 1. The averaged vector length for three routines that occupy more than 10% of the total CPU time are 240, which is close to the theoretical maximum value of 256 for each processor. In addition, the attained values of the flops for the top three routines reach 61%, 42%, and 61%, respectively, of the theoretical peak performance of 8 Gflops for each processor.

We employed one dimensional domain decomposition in the meridional direction for parallelization. Each processor is assigned computation in a zonal strip, and the number of meridional grid points in the zonal strip depends on the number of processors. As the number of processors increases, the meridional extent of a strip becomes comparable to or smaller than a halo region. This means that some device is necessary to reduce computational burdens especially in the halo regions.

In our model, autotasking techniques are used for intra-node parallelization, while inter-node communications were achieved via MPI library to get the best communication performance on the ES. The scaling performances of the tuned model with 4 halo regions are indicated in Table 2 as an example.

As a result of our tuning efforts, 100 years integration of our eddy-resolving simulation was estimated to be finished in 17 days CPU time with 1500 processors (188 nodes) on the ES.

4. Global aspects of simulated circulations

In order to examine basic capability of the model in reproducing the ocean circulations, several global aspects of the simulated results are shown in this section.

4.1. Sea surface height distribution

To assess the overall performance of the present high-

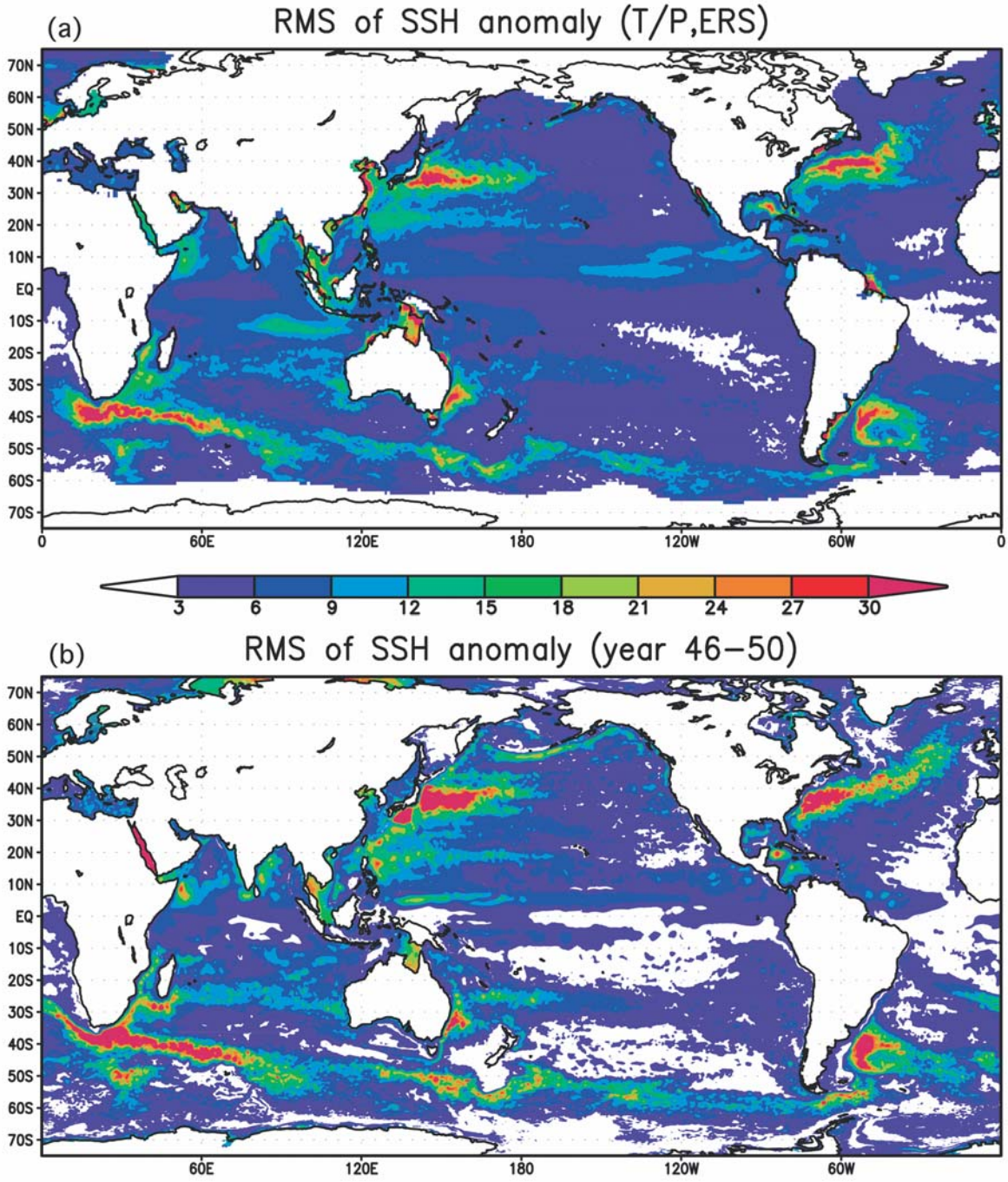

Fig. 3 Distribution of the root-mean-square variance of the sea surface height anomaly for (a) the observed and (b) the simulated variations. The simulated variance is calculated for 5-year time series from year 46 to 50. The observed variance is obtained from TOPEX/POSEIDON-ERS blended sea surface height anomaly data.

resolution OGCM, the five-year mean sea surface height (SSH) distribution over the whole model domain is shown in Fig. 1. The high SSH associated with subtropical gyres in the major basins and the low SSH regions near Antarctica and northern part of the North Atlantic Ocean can be seen as expected. In addition to this large-scale SSH distribution, wavy frontal structures in the Kuroshio-Oyashio confluence zone, in the Agulhas retroflexion area, and around the Antarctic Circumpolar Current (ACC) are well captured. Stationary coherent eddies and propagating eddies are also appeared in the western boundary current regions in the North Pacific, the North Atlantic, and the Agulhas Current region.

In Figure 2, showing a snapshot of SSH anomaly (SSHA) on April 1 of the 50th model year relative to the mean SSH, we notice that meso-scale eddy activities are ubiquitous even in the middle of the subtropical gyres, which is consistent with previous observational evidences

[15, 16]. The distribution of the root-mean-square variability of the simulated SSHA is compared well with that derived from TOPEX/Poseidon-ERS merged SSHA data in Fig. 3. Since the present model is driven by the climatological monthly forcing, the interannual variations in the observed SSHA are removed by subtracting one-year running-mean time series from the original variations.

There are five key regions where the SSHA variability is significantly large; the Gulf Stream, the Kuroshio, the Agulhas Current system, the East Australian Current, and

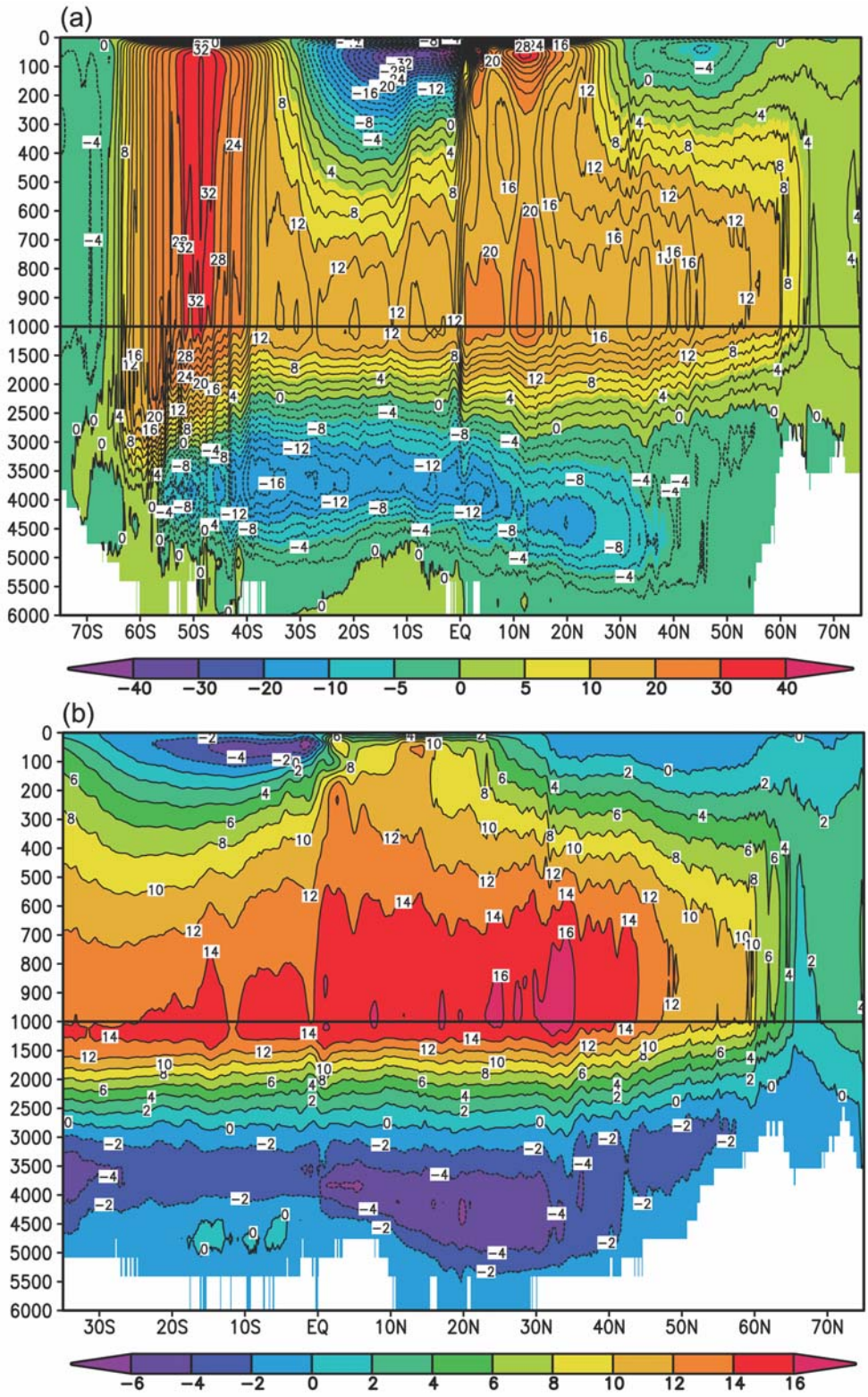

Fig. 4 Zonal mean vertical stream function (Sv = 10^6 m^3s^{-1}) for (a) Global and (b) Atlantic in the model.

the Brazil-Malvinas Confluence Zone. The amplitude and the distribution of the simulated SSHA variability appear to be realistic. These key regions basically correspond to the areas of energetic meso-scale eddy activity, some of which are described in detail in the following sections. It is worth mentioning here that the relatively large amplitude band associated with the Subtropical Countercurrent in the northwestern Pacific Ocean, extending zonaly around 20°N from the western boundary to near Hawaii, is well captured in the present model.

4.2. Meridional overturning

Annual mean meridional overturning stream function simulated in the model is shown in Fig. 4. The pattern and magnitude of the meridional overturning are similar to those from the other global ocean models [e.g. 1, 17] and the eddy-resolving models of the North Atlantic Ocean [e.g, 4, 18]. The results well capture shallow wind-driven cells in the upper ocean, the deep Deacon Cell in the Antarctic Circumpolar region, a strong northern thermohaline cell with sinking mostly in the North Atlantic, and the deep Antarctic Bottom Water (AABW) cell in the deep ocean (Fig. 4a). The magnitude of wind-driven subtropical cells reaches 37.4 Sv (1 Sv = 10^6 m^3s^{-1}) at 10°S and 33.4 Sv at 10°N, while the wind-driven cell in the northern subpolar region is 6.3 Sv at 45°N. The Deacon Cell in the Southern Ocean reaches down to about 3000 m depth, with the maximum transport of 34.5 Sv. It is of interest to point out that the present high-resolution model also captures the intense upwelling in the equatorial region, which could not be well reproduced in coarse resolution models.

Fig. 4b shows the meridional overturning stream function in the Atlantic Ocean. The cell for the North Atlantic Deep Water (NADW) has the maximum transport of 17.4 Sv at the depth of 900 m at 30°N. This NADW cell is slightly weaker and shallower than the result of Smith et al. [4], in which the maximum transport of the NADW cell occurs at 33.2°N, 1140 m depth with the magnitude of 23.9 Sv. However the southward transport of the NADW across the equator is nearly the same between the two models.

Fig. 5 demonstrates a longitude-depth section of the mean meridional velocity at 26.5°N west of Abaco Island in the Bahamas. The Deep Western Boundary Current is one of the important pathways of the meridional overturning cell, and it appears as a strong (up to 20 cm s^{-1}) and rather narrow (0.5° width) southward current close to the

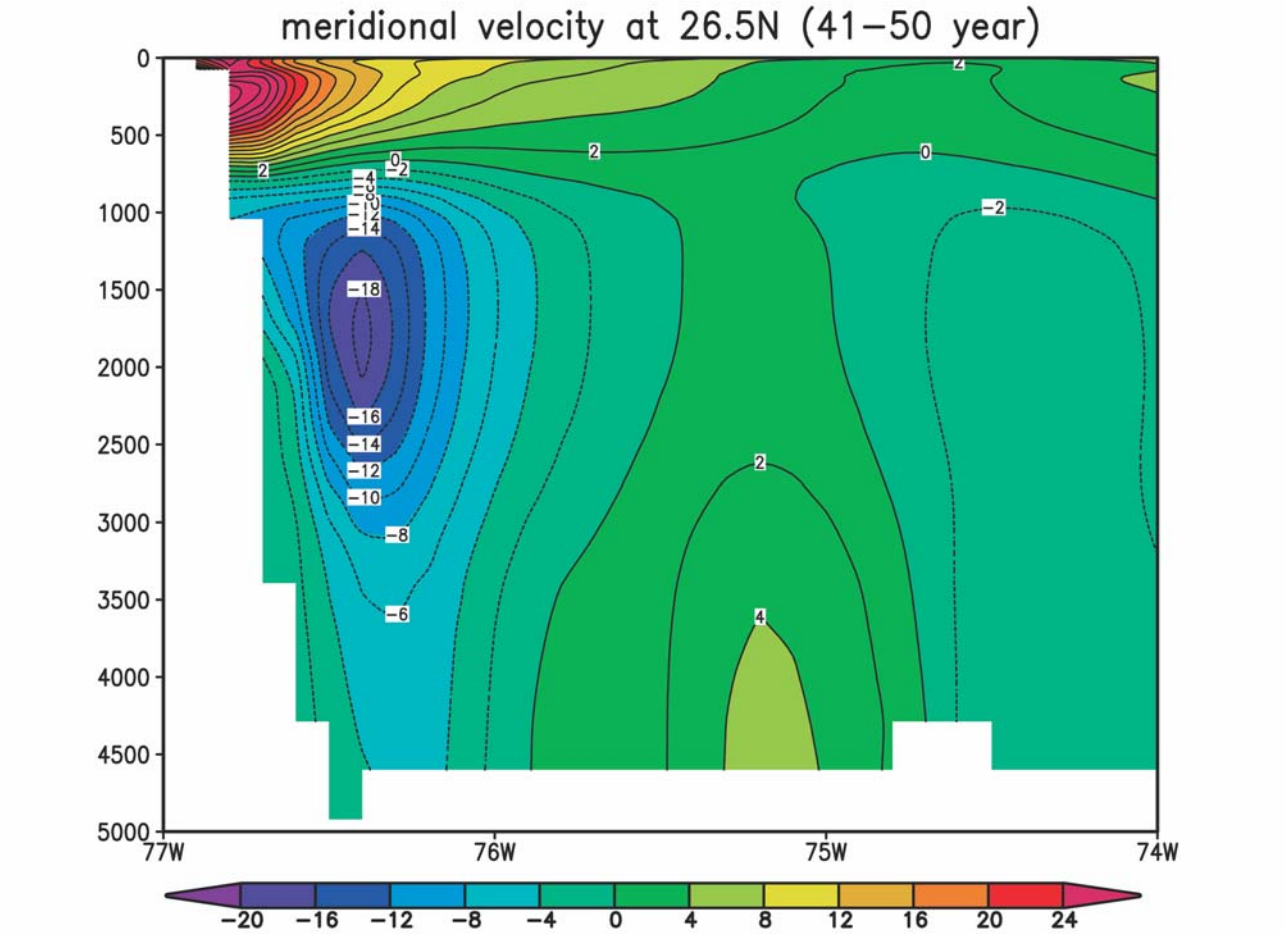

Fig. 5 Mean meridional velocity (cm s^{-1}) at 26.5°N.

western boundary beneath the northward surface current. The southward transport associated with this Deep Western Boundary Current is 24.8 Sv, which is in good agreement with the observation of Lee et al. [19]. Such a narrow current system is one of the good examples that can be simulated adequately only with the high-resolution models.

4.3. Comparison with WOCE hydrographic sections

Fig. 6 shows the simulated salinity distribution along P09 in the western North Pacific in July. There is a quite strong salinity front at 3°N, with the salinity maximum at the layer between 23.7σ_θ and 25.0σ_θ, which is consistent with the WHO [20]. This salinity maximum in the region

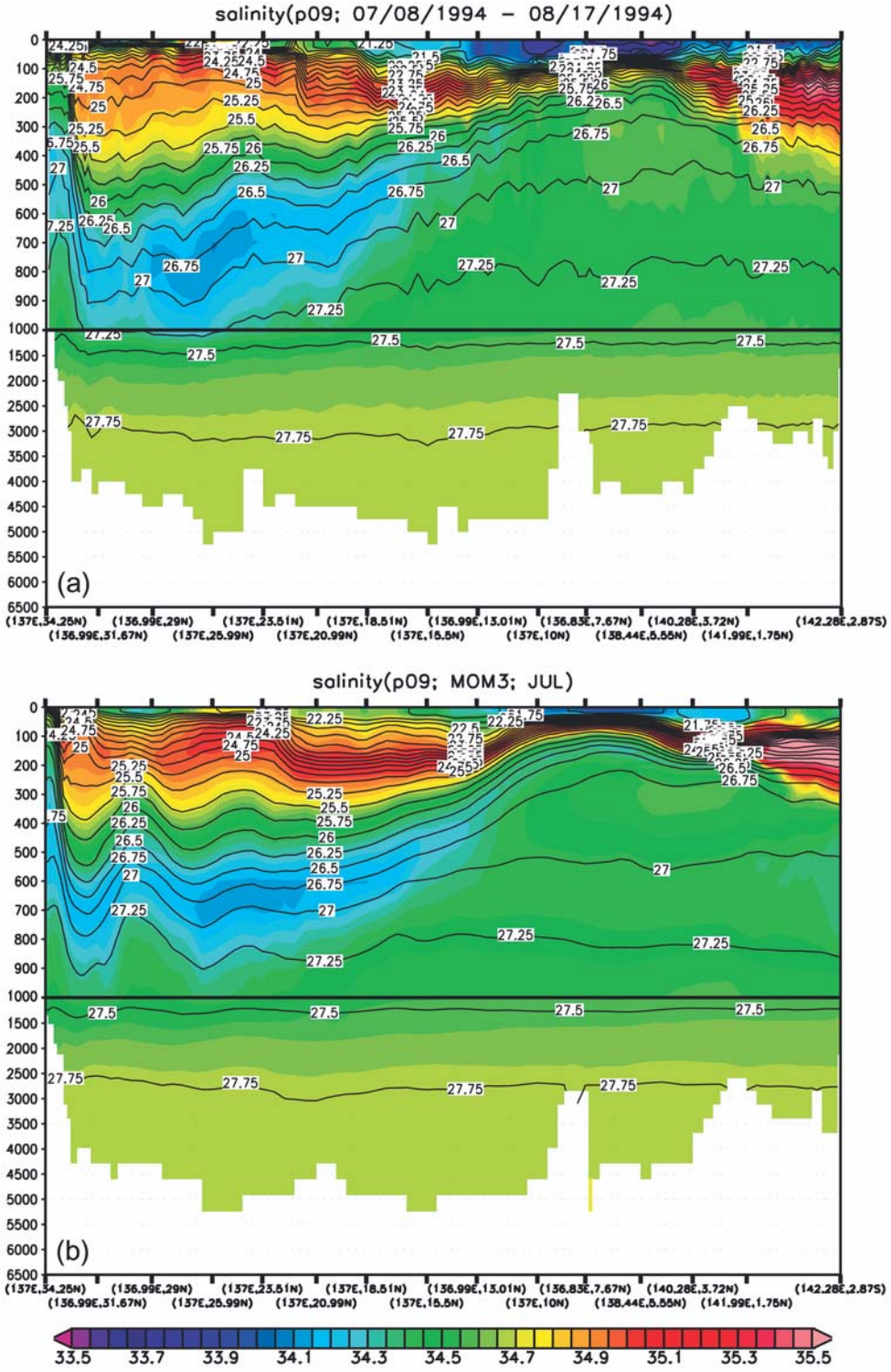

Fig. 6 Vertical cross section of the salinity (color) and potential density (contour) along P09 line obtained from (a) the WOCE hydrographic observation and (b) the model. Contour interval is 0.25 .

north of 3°N, known as the North Pacific Tropical Water, extends to about 24°N within the same density layer. The North Pacific Intermediate Water, characterized by the low salinity core less than 34.3 psu within a layer between $26.3\sigma_\theta$ and $27.2\sigma_\theta$, also extends southward to 15°N with realistic value of the salinity minimum. The results indicate that the high-resolution eddy-resolving OGCM has the ability to reproduce the appropriate distribution of the water masses with the simple bi-harmonic horizontal mixing instead of the isopycnal mixing scheme with the additional parameterization of Gent et al. [21].

In the eastern North Atlantic (A16N section), the typical water masses associated with the different salinity values are also reproduced by the present model (Fig. 7); those are

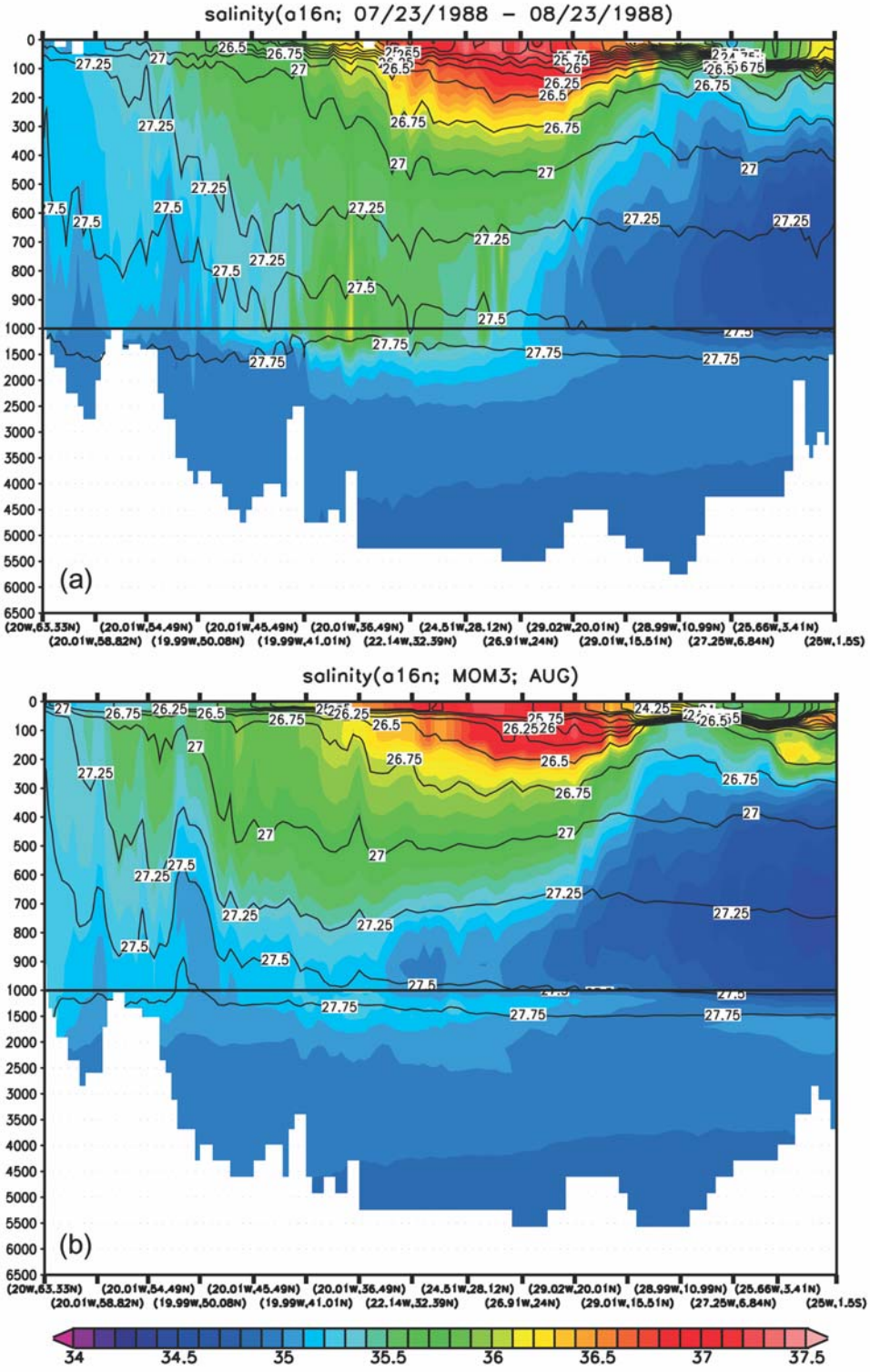

Fig. 7 As in Figure 6, but for A16N line.

the bowl-shaped surface saline water in the subtropical region, the North Atlantic Deep Water with the salinity of about 35 psu, and the Antarctic Intermediate Water (AAIW) with the salinity less than 34.9 psu. The salinity distribution corresponds well to the flow field indicated in the meridional overturning shown in Fig. 4b.

Fig. 8 shows the vertical cross section of the salinity along the I09N in the eastern Indian Ocean in boreal winter. Contrast between the low salinity water above the sharp halocline at about 50 m depth north of 15°S and the high salinity water in the southern hemisphere associated with the Indian Central Water are well reproduced in the

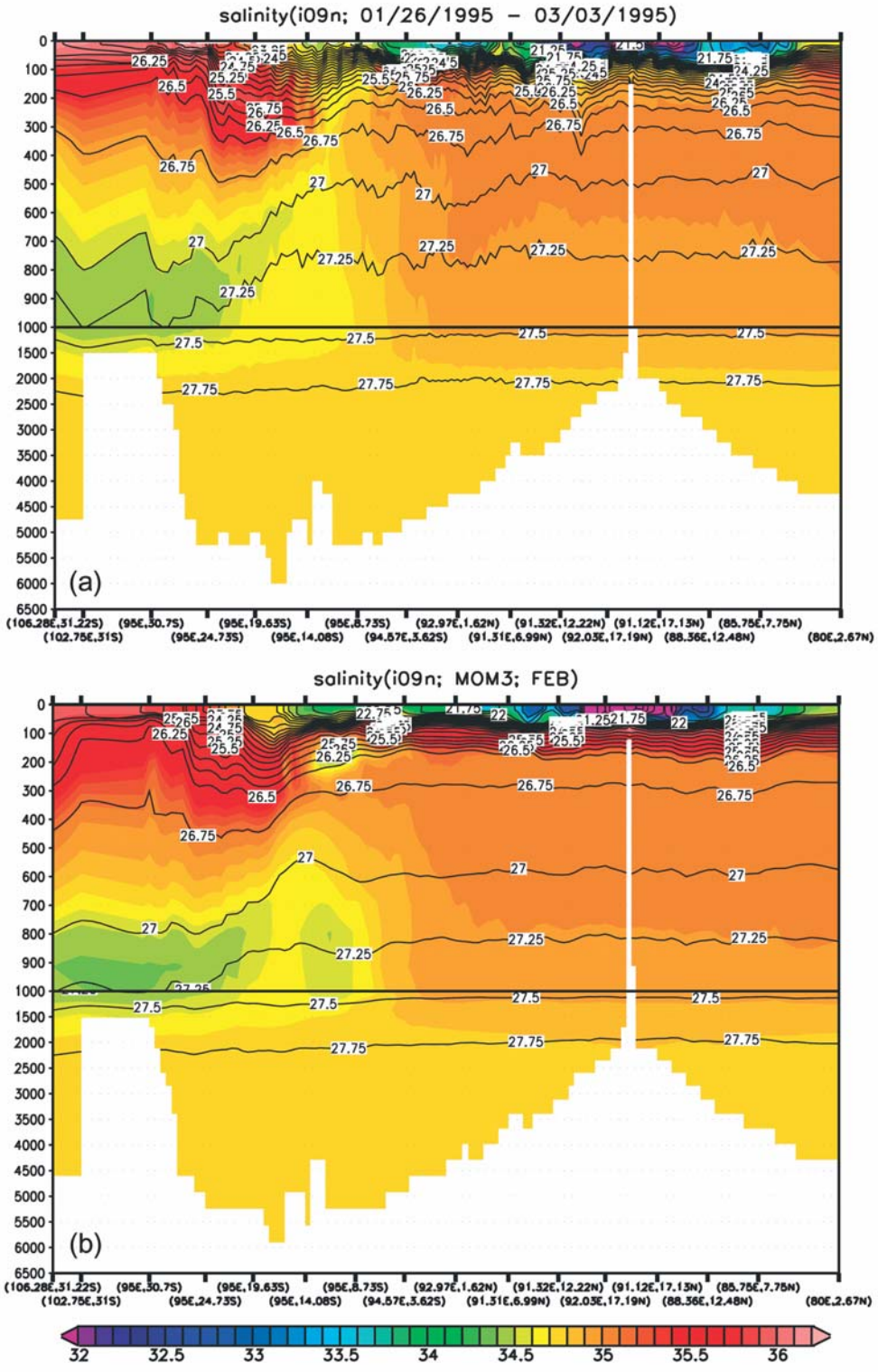

Fig. 8 As in Figure 6, but for I09N line.

model. Below the Indian Central Water, the salinity minimum layer corresponding to the AAIW is seen in the region south of 15°S. Note that the realistic bottom topography is adopted in the present model.

5. Regional circulations

We introduce here a close-up view for several important regions in the global ocean circulation. It is impossible to show the every detail of the variability in each region, but the followings can give us a flavor of the potential ability of the high-resolution global ocean simulations.

5.1. Kuroshio and Kuroshio Extension

Fig. 9 shows the SSH distribution in the Kuroshio/Kuroshio Extension region averaged over 5 years from year 46 to year 50. The simulated Kuroshio flows along the south coast of Japan and leaves from the coast for the Pacific interior at around 37°N, which is consistent with the observed separation latitude. Fig. 9 also demonstrates a triple frontal structure in the Kuroshio Extension/Oyashio region. Two of these form a single front in the Kuroshio Extension between 140°E and 155°E, with two stationary meanders, and bifurcate farther eastward; one extends to southeastward and another to the east up to 38°N. The other corresponds to the subpolar front that develops northeastward from 39°N near Japan to 44°N at the international dateline. This triple frontal structure is similar to observations from the satellite AVHRR (Advanced Very High Resolution Radiometer) infrared imagery [22] and to the hydrographic observation [23, 24].

Fig. 10 shows the composite of the monthly mean Kuroshio paths, defined by the location of the 14°C and 10°C isotherms at 300 m depth, during the year 46, together with the detailed bottom topography. One branch of the

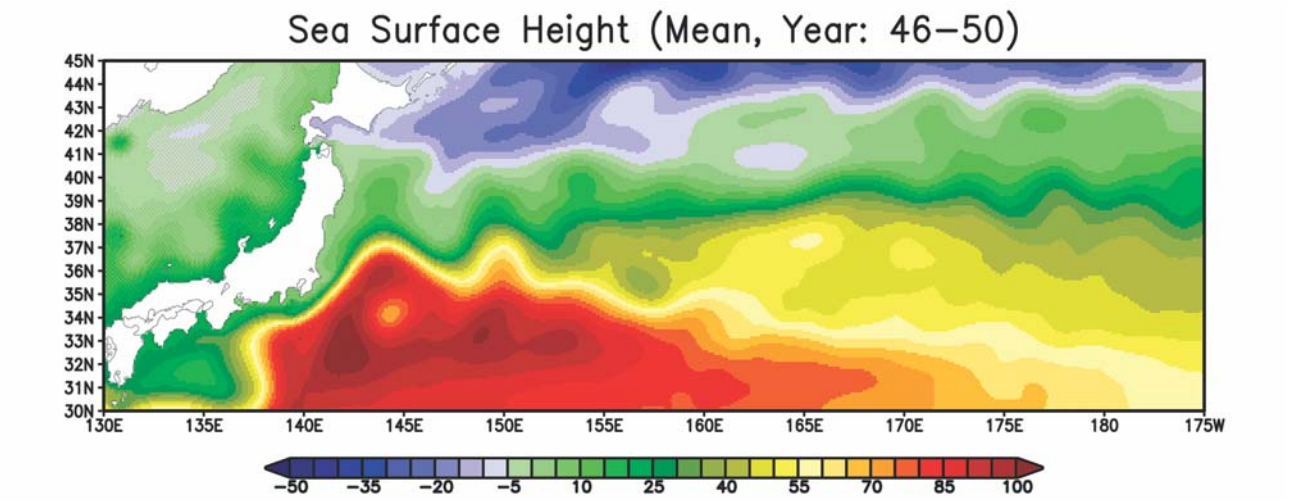

Fig. 9 Five-year mean field of sea surface height [cm] from year 46 to 50 around the Kuroshio/Oyashio region.

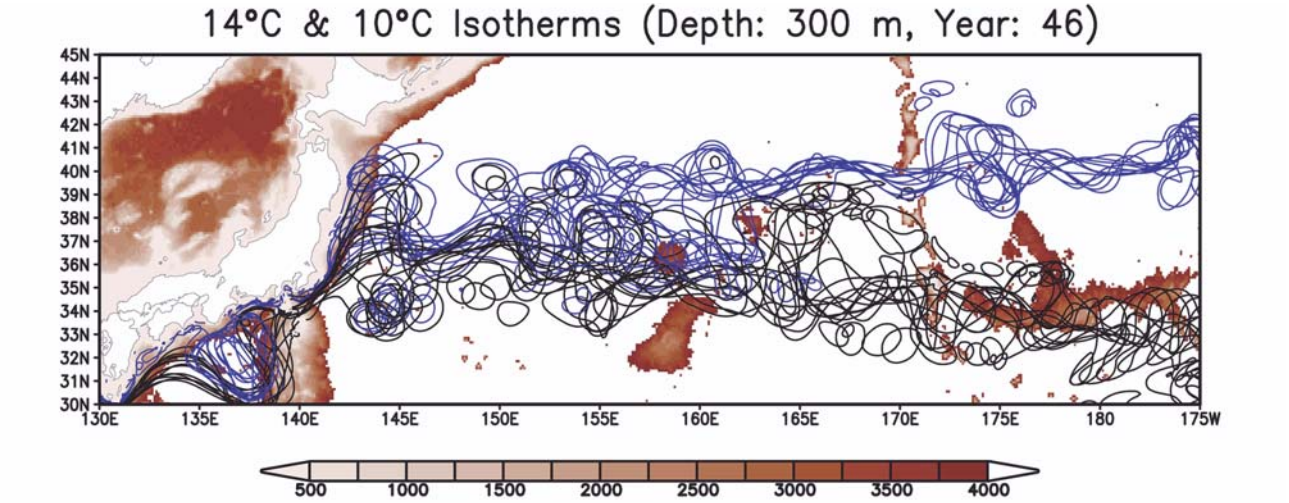

Fig. 10 Composite of the individual monthly-mean Kuroshio Current paths during the year 46, defined by the location at 300 m depth of the 14°C (black) and 10°C (blue) isotherms, superimposed upon the model bathymetry.

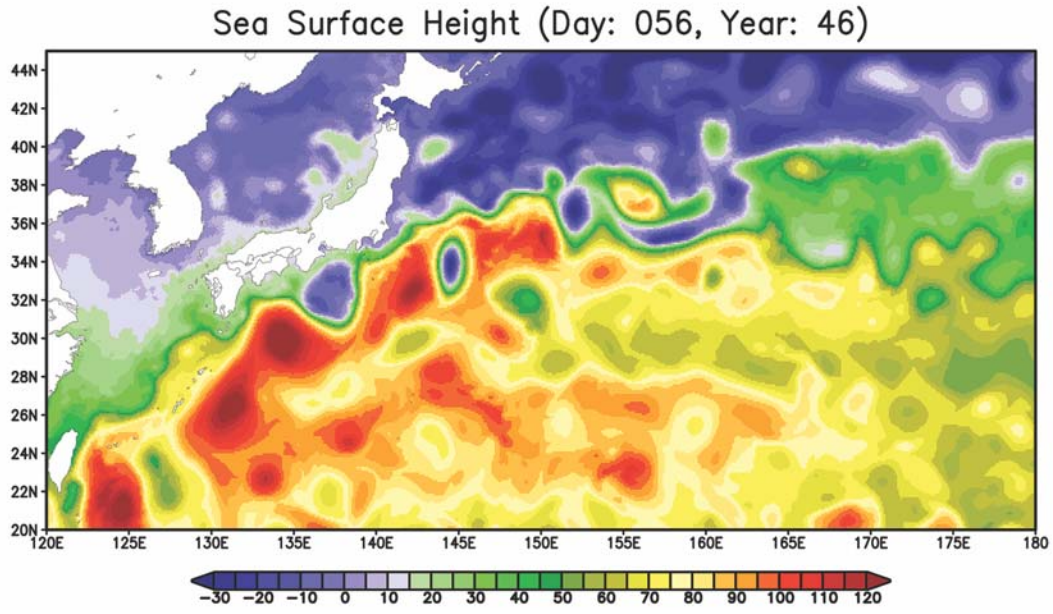

Fig. 11 Same as Figure 9, but for a snapshot on day 56 in the year 46.

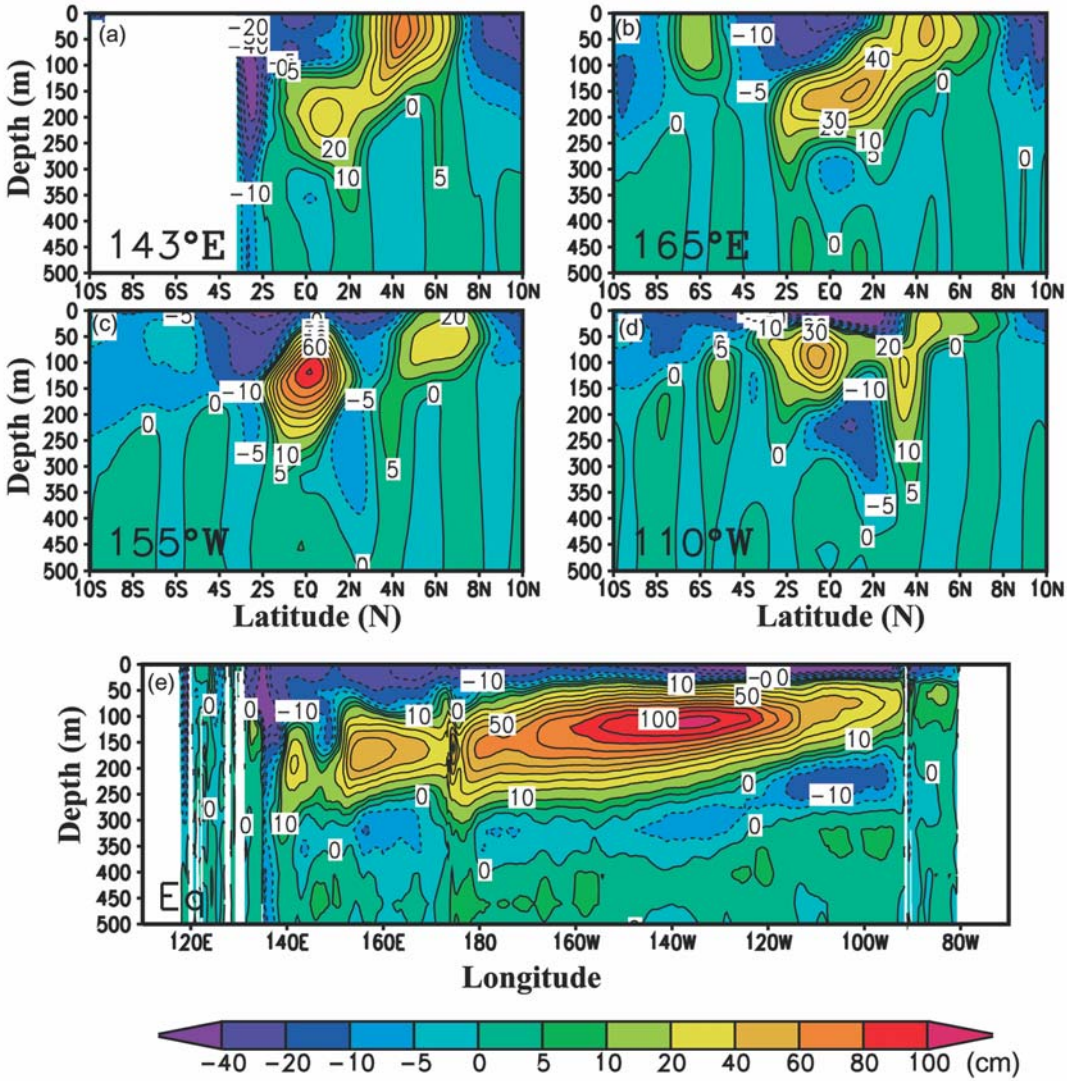

Fig. 12 Mean zonal velocity simulated in the model on meridional sections in the western (143°E, 165°E), central (155°W), eastern (110°W) Pacific Ocean and on the zonal section along the equator. Contour intervals are 10 cm s^{-1} and contour lines of +/- 5 cm s^{-1} are added.

Kuroshio Extension, shown by 10°C isotherms (blue curves), is oriented toward the northeast and passes south of the Nintoku Seamount of the Emperor Seamounts around 40°N, while the other extends eastward over the Hess Rise (black curves), showing the same frontal structures in the subsurface layer with that indicated in SSH distribution. This indicates the important role of the detailed structure of the bottom topography in determining the flow paths in the upper-layer, which is also suggested from the observations [e.g. 23, 25, 26].

Fig. 11 displays a snapshot of the simulated sea surface height field, exhibiting vigorous meso-scale eddy activities. A prominent feature is a series of anticyclonic recirculation gyres south of the Kuroshio and the Kuroshio Extension, whose area approximately overlaps with the region of the large SSHA variance (see Fig. 3). Recent satellite altimeter observation revealed that many anticyclonic and cyclonic eddies exist in the Kuroshio recirculation regions [e.g. 27, 28, 29]. There is another zonal band between 22°N and 26°N showing a series of the anticyclonic eddies, which propagate to the west along the subtropical front up to the Nansei Islands and Taiwan [30, 31, 32, 33]. These meso-scale eddies are believed to have significant impacts on the Kuroshio path variation south of Japan. The present model provides an ideal dataset to investigate such an interaction between the meso-scale eddies and the western boundary current.

5.2. Equatorial currents in the Pacific Ocean

The Hawaii-to-Tahiti Shuttle experiment [34] provides us one of the most useful data to validate the simulated current structures of the equatorial Pacific Ocean. The observed structures are updated recently by Johnson et al. [35], in which the direct estimates of the zonal currents and contemporaneous hydrographic data are combined. The meridional sections of mean zonal currents at four different longitudes and a zonal section along the equator simulated in the model (Fig. 12) are in good agreement with such observed equatorial current systems, including the Equatorial Undercurrent (EUC) and the other series of alternating jets; the North Equatorial Countercurrent (NECC), the Subsurface Countercurrents (SCCs), and the two major westward currents of the South Equatorial Current (SEC) and the Equatorial Intermediate Current (EIC).

The EUC starts at around 150°E and strengthens downstream, having two major maxima at 140°W, 120m depth and 155°E, 160m depth. It is interesting to note that the magnitude of the EUC weakened around 165°E, which is also shown in the observed data by Johnson et al. [36]. Another local maximum in eastward velocity at 140°E at 200m depth corresponds to the returning flow of the New Guinea Coastal Undercurrent (NGCUC), which has maxi-

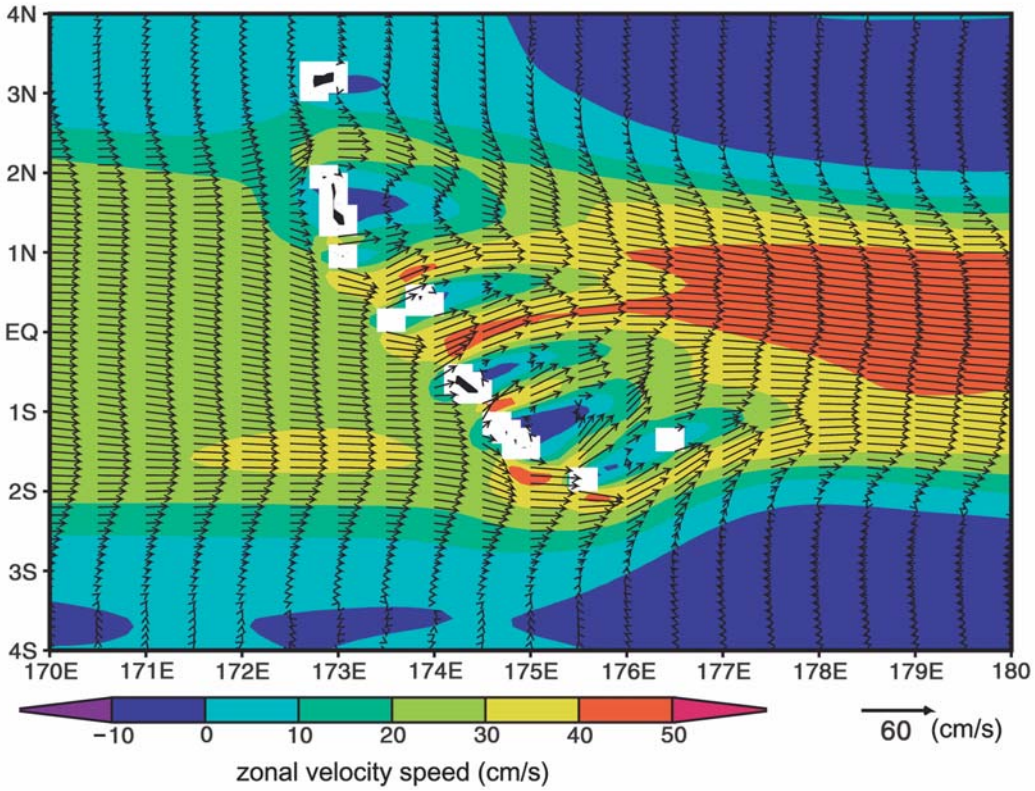

Fig. 13 Mean horizontal velocity vectors around the Gilbert Islands at near the depth of the model EUC core (207m).

mum westward current of about 50 cm s^{-1}. The model also shows a local maximum of the zonal current around 175°E where the EUC is divided into several swift jets upon reaching the narrow passages between the Gilbert Islands (Fig. 13). The model EUC shows significant changes in its magnitude and meridional width in the zonal direction across the islands. This suggests the islands may regulate the flow pattern in relatively large area, and, in particular, play an important role for the retardation of the EUC west of the islands.

The SCCs are also simulated though the maximum velocities are slightly weaker than the observed values. The model reproduces zonal variations of the structure of the SCCs as well. They flow at around 2°N and 2°S as two narrow currents connecting to the bottom of the EUC in the western region, then, they shift their cores poleward as they move to the east, flowing along 4°N and 4°S as the currents clearly separated from the EUC in the central Pacific. This structure accompanies the layer of rather uniform density in vertical, known as the pycnostad, below the thermocline, which develops from west to east, as reported in the data analysis of Johnson and Moore [37]. The very high horizontal and vertical resolution may be a key parameter for this successful simulation.

5.3. Indonesian throughflow

Another example to show the advantage of using the high-resolution global-domain OGCM can be seen in the Indonesian throughflow area, where the flows through narrow passages between the islands, scattering within the Indonesian Seas, provides a choke region of the global-scale circulations. The simulated net transport of the

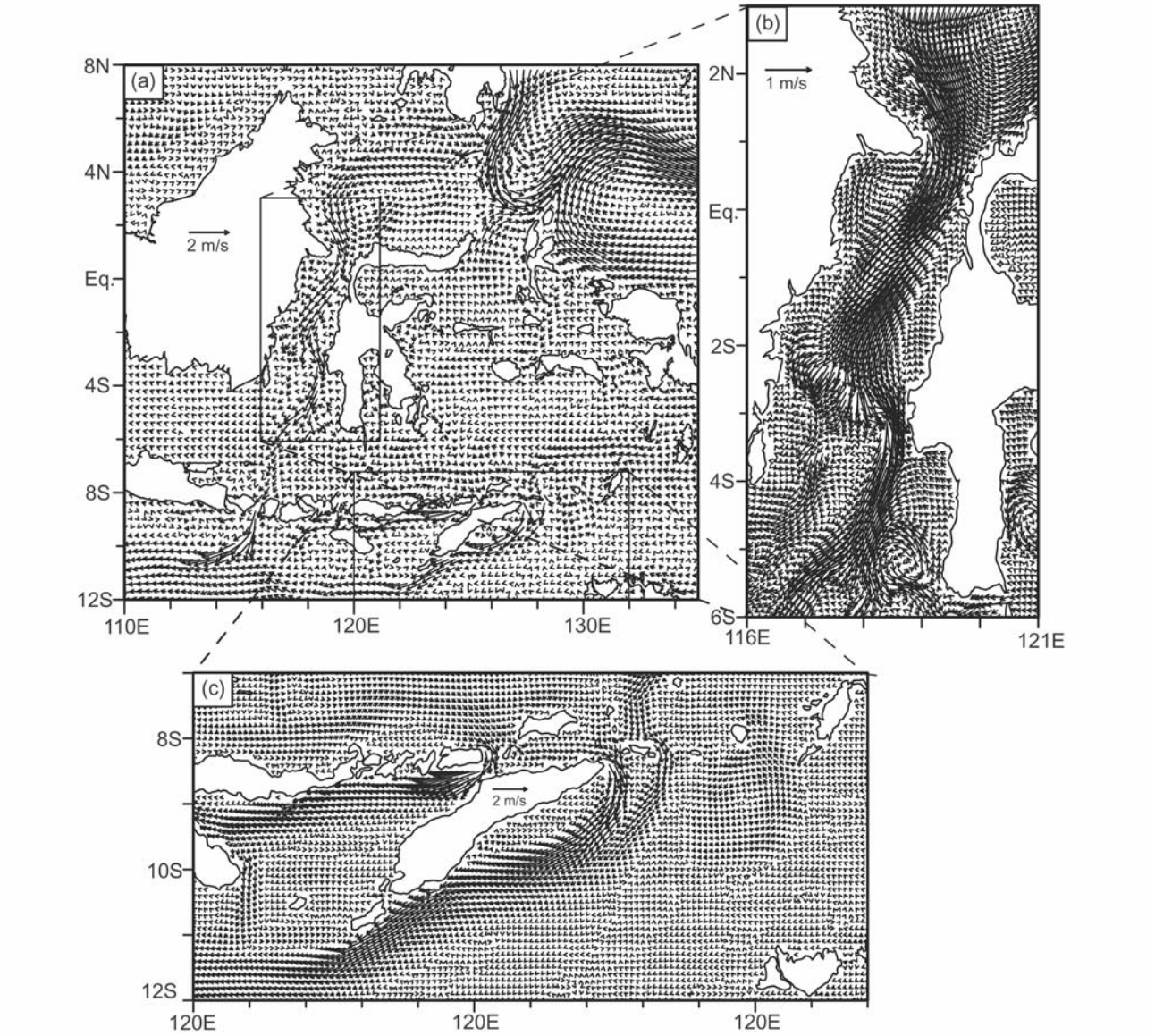

Fig. 14 (a) Monthly mean surface velocity field on August in the Indonesian archipelago, (b) the enlarged view around the Macassar Strait, and (c) the close-up of the velocity distribution around the Timor Island.

Indonesian throughflow has the annual mean of 9.2 Sv from the Pacific to the Indian Ocean, with the seasonal amplitude of 17.6 Sv. The maximum (minimum) transport from the Pacific to the Indian Ocean occurs in July (November), which is consistent with the previous observations and model simulations [e.g. 38, 39, 40, 1]. Fig. 14a indicates the monthly mean surface flow field within the Indonesian Seas in August. It is clearly seen that the main route of the surface throughlow passes through Macassar Strait and several passages within the Lessar Sunda Islands. The model can capture the detailed structure of the flow in the Macassar Strait, such as a quite narrow southward flow regulated by the bottom topography in the eastern part of the strait at 3°S and an anticlockwise eddy of the horizontal scale of 100 km at 5°S, even in the monthly mean field. The results also demonstrate a complex flow field around the Timor Island (Fig. 14c), showing the potential ability for the study about the interaction among the small-scale circulations, the topography within the Indonesian Seas, and the Indonesian throughflow.

5.4. Wyrtki Jets and Great Whirl in the Indian Ocean

Fig. 15 shows the longitude-time section of the surface zonal current along the equator in the Indian Ocean. Twice a year, during the monsoon transition periods in spring and fall, eastward jets, known as Wyrtki jets, appear along the equator [41, 42]. Maximum speed of the Wyrtki Jets in the present model is about 80 cm s^{-1} and is somewhat weaker than the observed value of over 100 cm s^{-1} [43]. Note that there is a jump in the amplitude around 73°E, which is caused by the shallow topography associated with the Maldive Islands. Han et al. [43] report from their numerical model that the Maldive Islands reduce the amplitude of the Wyrtki jets by up to 20 cm s^{-1}.

Fig. 16 shows sequential development of the Somali current system over the course of a year. As the Southwest monsoon develops (from Fig. 16a to Fig. 16b), the cross-equatorial western boundary current reverses to northward, and the two prominent gyres appear; the Great Whirl at 4°–10°N and the Southern Gyre at 2°N–2°S [44]. Two wedge-shaped cool SST regions attached to the African coast, with very sharp frontal structure along the northern edge of the gyres, compares well with the observations [cf. 44, 45]. There is another frontal structure in the SST field along the offshore side of the gyres around 52°E to 56°E in June, together with many meso-scale eddy structures. The ensuing development and decay of the Great Whirl are also well reproduced in the model [cf. 46, 47].

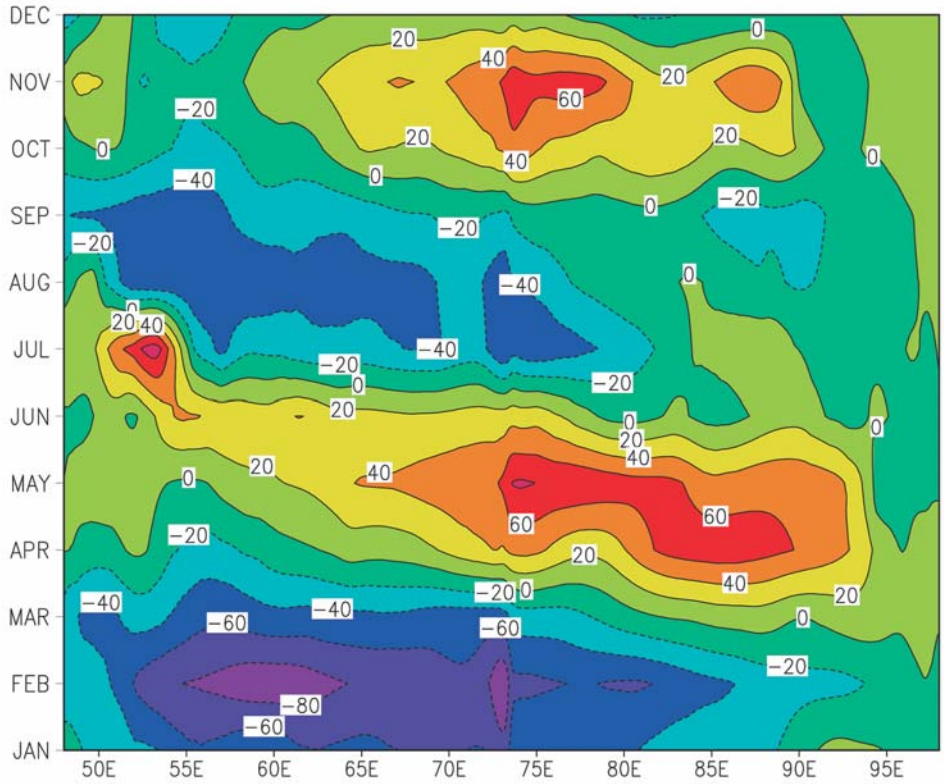

Fig. 15 Longitude–time plot of the zonal velocity at the equator in the Indian Ocean. The contour interval is 20 cm s^{-1}. Plot is made from the monthly average values.

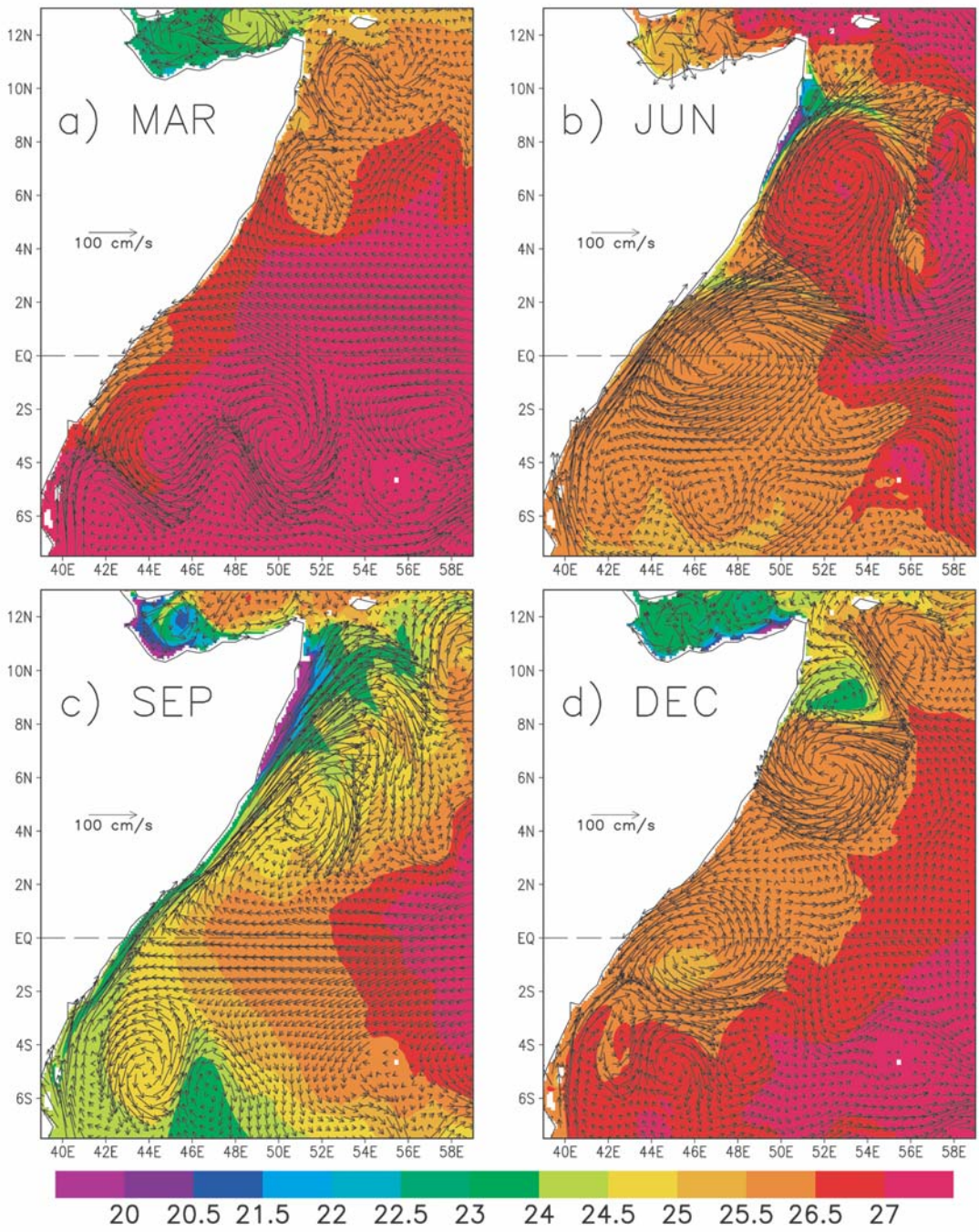

Fig. 16 Seasonal sequence of the Somali Current system in a) March b) June c) September d) December. Vectors are zonal velocities at 25 m depth. Contour is for the sea surface temperature. Data are from the monthly averages.

5.5. Agulhas current system

The annual mean surface height field in the southwestern Indian Ocean around the Agulhas Current system is shown in Fig. 17. In the annual mean field, two upstream currents originated from the South Equatorial Current are recognized as sources of the Agulhas Current. These are the Mozambique Current, flowing to the south along the east African coast, and the East Madagascar Current off the east coast of the Madagascar Island. However, due to large temporal variability associated with the eddy activities, these two currents are hardly identifiable in an instantaneous flow field. They manifest themselves as currents only in the time mean field. The annual mean total volume transports of the Mozambique Current across the section at 23°S and the East Madagascar Current across the section between the southern tip of Madagascar and 29°S, 49°E (see Fig. 17) are about 14 Sv and 34 Sv, respectively. On the other hand, the transport off the southeastern coast of South Africa at around 27°E reaches 98 Sv. This large transport at the downstream region is associated with the

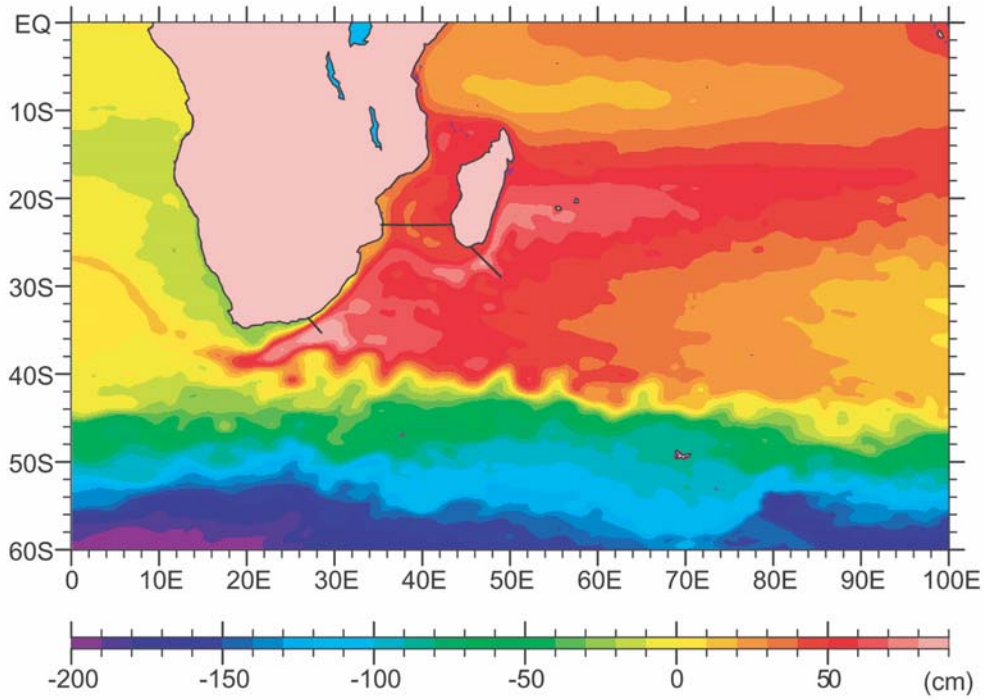

Fig. 17 Annual mean field of the sea surface height in the southwestern Indian Ocean. Contour interval is 10 cm. The black solid lines across the Agulhas current system off the coast of Africa and Madagascar indicate the sections where the volume transport are calculated.

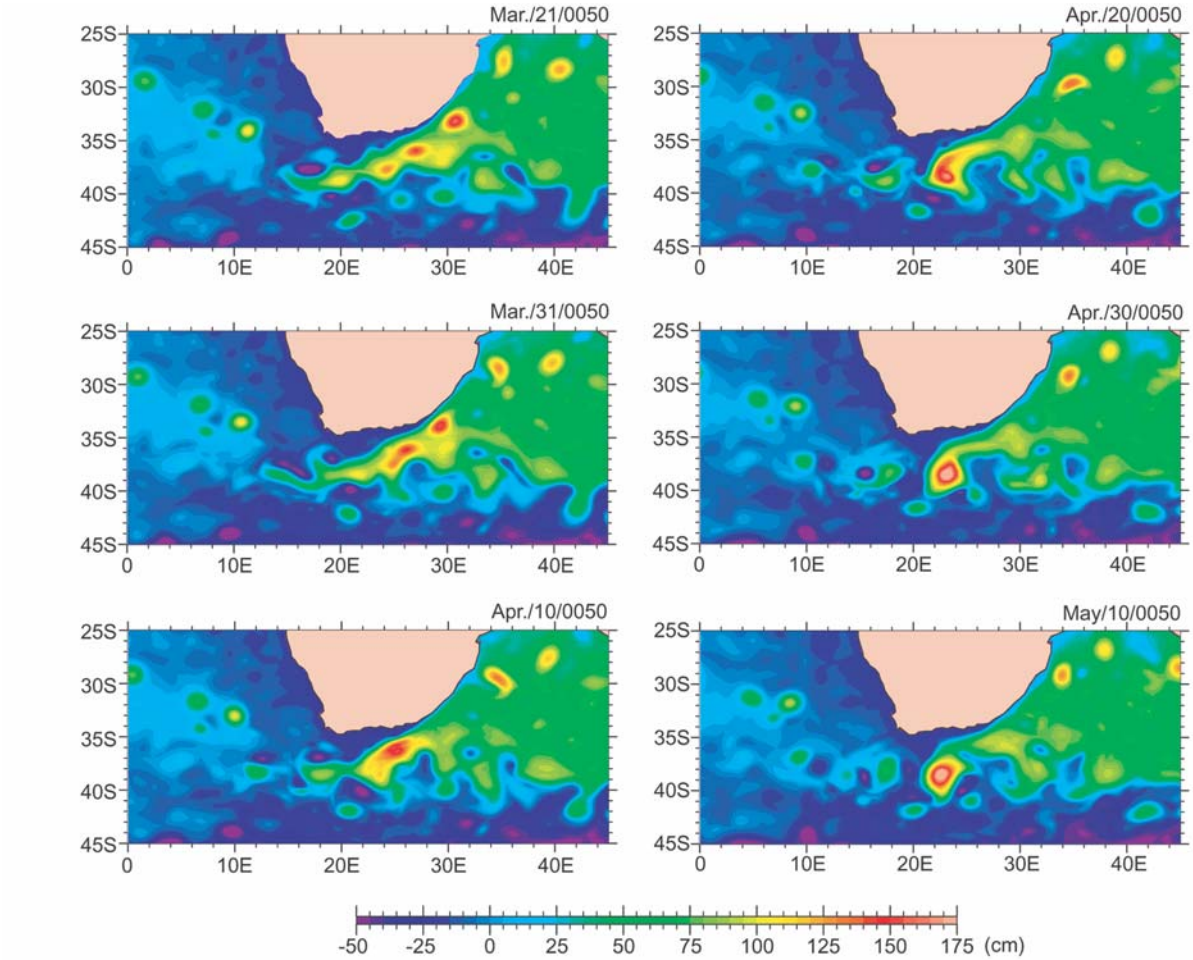

Fig. 18 Time sequence of the sea surface height anomaly in every 10 days for the region near the southern tip of Africa.

recirculation gyre called the Southwest Indian Ocean subgyre [48], where the meso-scale eddy activity is rather strong (see Fig. 18).

Fig. 18 demonstrates a time sequence of the SSHA around the Agulhas retroflection area from March 21 to May 10 of the model year 49 in every 10 days. The western tip of the retroflection, where the current tightly turns back to the east, is fairly variable in relation with the generation of the anticlockwise meso-scale eddy, known as the Agulhas Ring. The number of eddies generated in the present model is 5 or 6 per year, which is similar to the result of FRAM experiment [3] and the observations [49]. However, the simulated diameter of each ring in the present model is about 300 km, which is much closer to the observed value of 220 km, comparing to the value of 450 km of the FRAM result.

5.6. Antarctic Circumpolar Current (ACC)

One of the interesting regions to see the relation between the local topography and the global circulation is the Drake Passage for Antarctic Circumpolar Current (ACC). The monthly volume transport of ACC across the Drake Passage, averaged over 10 years from the 41st to 50th model year, is indicated in Fig. 19. The simulated annual mean transport is 152.5 Sv, which is slightly larger than the observed value of 130 Sv [50]. The semiannual signal with maximum transport in March and October has the amplitude of 2.5 Sv, which is again similar to the observation of Whitworth and Peterson [50]. Also indicated in Fig. 19 is the maximum zonal mean value of the monthly zonal wind stress between 40°S and 75°S around the ACC region. The zonal wind stress also shows distinct semiannual signal, suggesting the importance of the wind stress on the variability in the ACC transport.

A number of circumpolar fronts, which form the water mass boundaries and often accompany narrow jet-like current structure, observed in the Southern Ocean are clearly reproduced in the model. Fig. 20 shows the annual mean temperature gradients and the magnitude of the horizontal velocity at the depth of 100 m, reflecting complicated frontal structures even in the annual mean fields. The map of the salinity gradients (not shown) indicates basically the same structure with that in Fig. 20a. The locations of Subantarctic and Polar fronts, Southern front, and Southern boundary of ACC are similar to those derived from satellite remote sensing [51, 52] and in-situ hydrographic observations [53]. The Antarctic Slope Front, found along westward flow near the continental margin of the Antarctica [54] is also identified in the simulated results. Similarity between the two fields in Fig. 20 suggests that the gradients of the tracer fields can be a good indicator of the position of the narrow jets at 100 m depth in the ACC region.

6. Summary and Discussion

A fifty-year simulation with the climatological forcing using a high-resolution ocean general circulation model

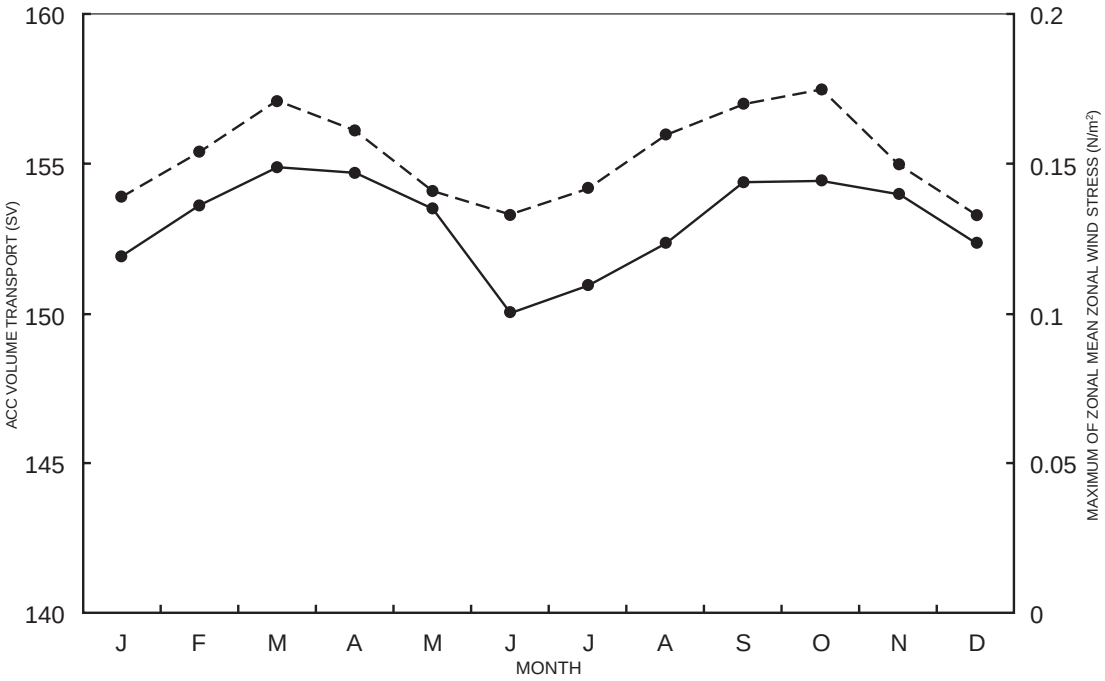

Fig. 19 Solid line: Monthly mean volume transport (Sv) of Antarctic Circumpolar Current across the Drake Passage averaged over 10 years from model year 41 to 50. Dashed line: Maximum value of zonal mean monthly zonal wind stress between 40°S and 75°S.

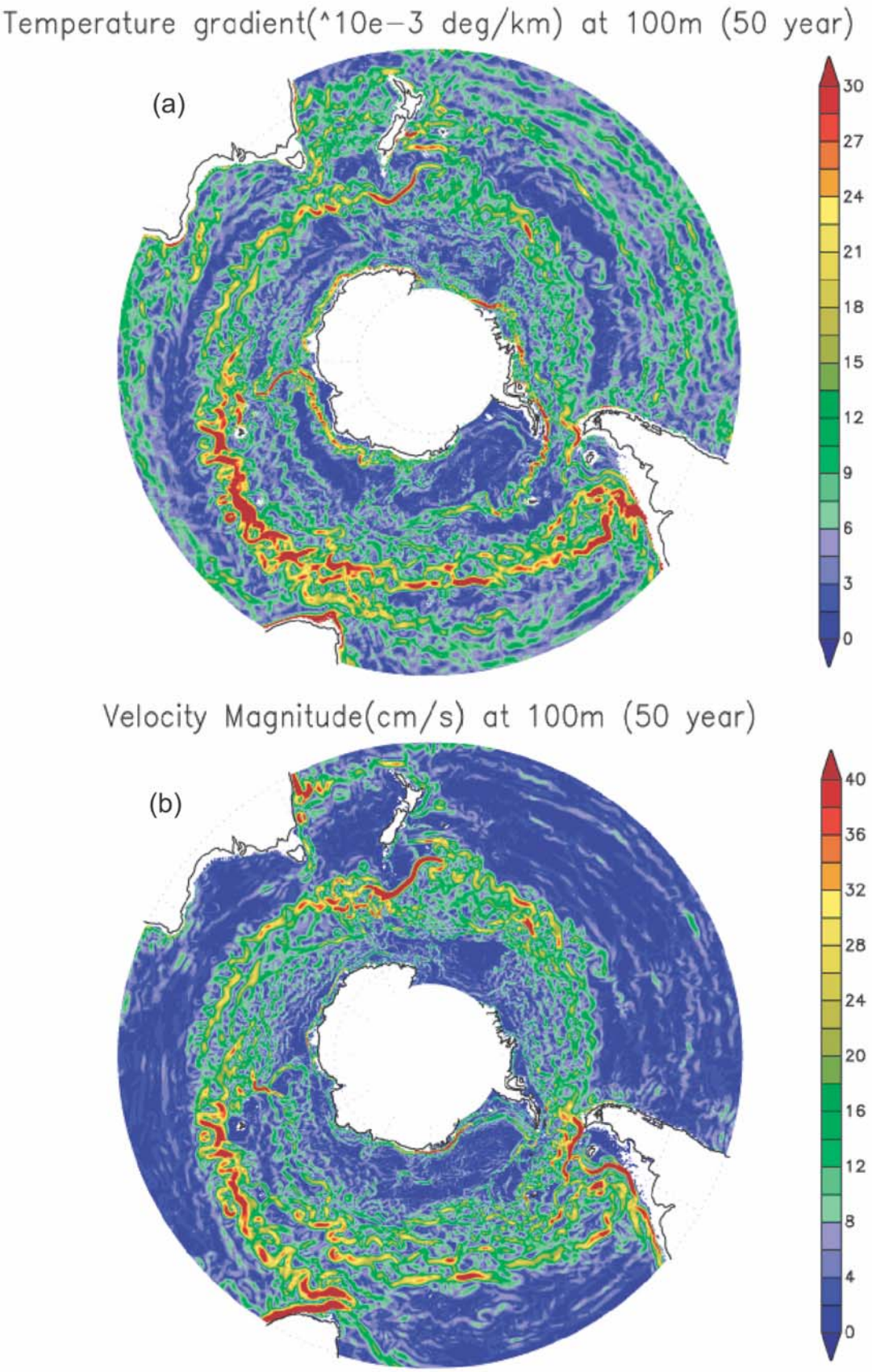

Fig. 20 Annual mean distribution of (a) the temperature gradients and (b) the magnitude of the horizontal velocity at the depth of 100 m in the Antarctic Circumpolar Current region.

has been performed on the Earth Simulator (ES), and some of the preliminary results are highlighted. The model adopts the horizontal grid spacing of 1/10° with 54 vertical levels and is specifically tuned for the ES. The fifty-year simulation has been finished within a month.

The statistical analysis indicates that the magnitude and spatial distribution of the sea surface height variability is consistent with those observed by satellite altimetries, especially in the regions with the large amplitude near the western boundary currents in the major basins. The model results also capture realistic variations in the velocity and tracer fields associated with the meso-scale eddy activities as well as the seasonal variations of the large-scale circulations. The above preliminary results indicate that the super-high resolution ocean general circulation model can be a powerful tool for investigating not only the large-scale ocean circulations but also the relatively small-scale phenomena, such as the meso-scale eddies and the instability of the currents, and the interactions between the phenomena in the different spatial and temporal scales. Our simulation demonstrates the potential ability of such high resolution simulations for better understanding of the sub-grid phenomena, which are somehow parameterized or not well resolved in the coarser resolution models.

Separation of western boundary currents such as the Kuroshio and the Gulf Stream from the coast has been an outstanding problem in numerical ocean models. The Kuroshio in the previous simulations often overshoots up to the latitude of about 40°N where the subpolar front exists in reality [e.g. 1]. Although the problem has not been clearly solved, recent numerical studies suggest that the refinement of horizontal resolution can be a possible remedy for the issue [55, 4]. The fact that the Kuroshio in our simulation separates from the coast at the correct latitude (see Fig. 9) supports the above idea and is consistent with their suggestion that a grid spacing of finer than 1/10° is required in order to represent the realistic separation of western boundary currents.

Another important aspect resulted from the refinement of horizontal and/or vertical resolution is the interaction between the bottom topography and the relatively small-scale current system [cf. 56]. Once the model resolution becomes high enough to resolve the baroclinic Rossby radius (about 30 km) in the mid-latitude, the baroclinic instability yields bottom currents properly. These currents then interact with bottom topography, which is also represented realistically in the high-resolution model, and the surface currents are regulated by these interactions.

While the present model captures many aspects of the ocean circulations and their variability in some detail, several issues still need to be addressed to minimize significant differences from the observed data. For example, the simulated mixed-layer depth in the subarctic region north of about 40°N in the Pacific Ocean is too shallow. The Kuroshio has sometimes a large meandering path off the coast of Kyushu Island, Japan, which is too far west compared with the canonical large-meander that appears near the Kii Peninsula. To overcome these issues, a different type of the parameterization in the sub-grid scale mixing processes may be required. In addition, the tidal currents and the nonhydrostatic processes should be included in the future version of the high resolution model for much better simulations within the marginal seas, the coastal areas, and the polar regions.

Together with the accompanying high-resolution atmospheric general circulation model [57], a high-resolution coupled simulation is feasible on the Earth Simulator. Detailed analyses of the results from these models and the OFES will contribute to pushing the frontier of the climate research further ahead.

Acknowledgment

The authors are deeply indebted to the late Dr. Miyoshi for his tremendous effort put in for the realization of the Earth Simulator. The present article is dedicated to his great spirit. We also thank Messrs. Tsuda, Kanazawa, and Kitawaki for their efforts to develop the best parallelization and optimization scheme of the original code for the Earth Simulator.

(This article is reviewed by Dr. Julia Slingo.)

Refernces

[1] A. J. Semtner, and R. M. Chervin, Ocean general circulation from a global eddy-resolving model, *J. Geophys. Res*., vol.97, pp.5493–5550, 1992.

[2] P. Saunders, and S. R. Thompson, Transport, heat and freshwater fluxes within a diagnostic model (FRAM), *J. Phys. Oceanogr*., vol.23, pp.452–464, 1993.

[3] J. R. E. Lutjeharms, and D. J. Webb, Modelling the Agulhas Current system with FRAM (Fine Resolution Antarctic Model), *Deep-Sea Res*., vol.42, pp.523–551, 1995.

[4] R. D. Smith, M. E. Maltrud, F. O. Bryan, and M. W. Hecht, Numerical simulation of the North Atlantic Ocean at 1/10, *J. Phys. Oceanogr*., vol.30, pp.1532–1561, 2000.

[5] D. J. Webb, Evidence of shallow zonal jets in the South Equatorial Current region of the Southwest Pacific, *J. Phys. Oceanogr*., vol.30, pp.706–720, 2000.

[6] R. C. Pacanowski, and S. M. Griffies, *MOM 3.0 Manual*, Geophysical Fluid Dynamics Laboratory/National Oceanic and Atmospheric Administration, 680pp., 2000.

[7] W. G. Large, J. C. McWilliams, and S. C. Doney, Oceanic vertical mixing: A review and a model with a nonlocal

boundary layer parameterization, *Rev. Geophys*., vol.32, pp.363–403, 1994.

[8] A. Rosati, and K. Miyakoda, A general circulation model for upper ocean circulation, *J. Phys. Oceanogr*., vol.18, pp.1601–1626, 1988.

[9] T. P. Boyer, S. Levitus, J. I. Antonov, M. E. Conkright, T. O'Brien, and C. Stephens, *World Ocean Atlas 1998 Vol. 4: Salinity of the Atlantic Ocean, NOAA Atlas NESDIS 30*. U.S. Government Printing Office, Washington, D.C., 1998a.

[10] T. P. Boyer, S. Levitus, J. I. Antonov, M. E. Conkright, T. O'Brien, and C. Stephens, *World Ocean Atlas 1998 Vol. 5: Salinity of the Pacific Ocean, NOAA Atlas NESDIS 31*. U.S. Government Printing Office, Washington, D.C., 1998b.

[11] T. P. Boyer, S. Levitus, J. I. Antonov, M. E. Conkright, T. O'Brien, C. Stephens, and B. Trotsenko, *World Ocean Atlas 1998 Vol. 6: Salinity of the Indian Ocean, NOAA Atlas NESDIS 32*. U.S. Government Printing Office, Washington, D.C., 1998c.

[12] J. I. Antonov, S. Levitus, T. P. Boyer, M. E. Conkright, T. O'Brien, and C. Stephens, *World Ocean Atlas 1998 Vol. 1: Temperature of the Atlantic Ocean, NOAA Atlas NESDIS 27*. U.S. Government Printing Office, Washington, D.C., 1998a.

[13] J. I. Antonov, S. Levitus, T. P. Boyer, M. E. Conkright, T. O'Brien and C. Stephens, *World Ocean Atlas 1998 Vol. 2: Temperature of the Pacific Ocean, NOAA Atlas NESDIS 28*. U.S. Government Printing Office, Washington, D.C., 1998b.

[14] J. I. Antonov, S. Levitus, T. P. Boyer, M. E. Conkright, T. O'Brien, C. Stephens, and B. Trotsenko, *World Ocean Atlas 1998 Vol. 3: Temperature of the Indian Ocean, NOAA Atlas NESDIS 29*. U.S. Government Printing Office, Washington, D.C., 1998c.

[15] MODE Group, The Mid-Ocean Dynamics Experiment, *Deep-Sea Res.*, vol.25, pp.859–910, 1978.

[16] L.-L. Fu, and R. D. Smith, Global Ocean Circulation from Satellite Altimetry and High-Resolution Computer Simulation, *Bull. Amer. Meteor. Soc*., vol.77, pp.2625–2636, 1996.

[17] M. E. Maltrud, R. D. Smith, A. J. Semtner, and R. C. Malone, Global eddy-resolving ocean simulations driven by 1985-1995 atmospheric winds, *J. Geophys. Res*., vol.103, pp.30825–30853, 1998.

[18] J. Willebrand, B. Bariner, C. Booning, C. Dieterich, P. D. Killworth, C. Le Provost, Y. Jia, J.-M. Molines, and A. L. New, Circulation characteristic in three eddy-permitting models of the North Atlantic, *Prog. Oceanogr*., vol.48, pp.123–161, 2001.

[19] T. N. Lee, W. E. Johns, R.J. Zantopp, and E. R. Fillenbaum, Moored observations of western boundary current variability and thermohaline circulation at 26.5N in the subtropical North Atlantic, *J. Phys. Oceanogr*., vol.26, pp.962–983, 1996.

[20] F. M. Bingham, T. Suga and K. Hanawa, The origin of waters observed along 137°E, *Int'l WOCE Newslett*., vol.36, pp.26–27, 1999.

[21] P. R. Gent, J. Willebrand, T. McDougall, and J. C. McWilliams, Parameterizing eddy-induced tracer transports in ocean circulation models, *J. Phys. Oceanogr*., vol.25, pp.463–474, 1995.

[22] J. L. Mitchell, W. J. Teague, G. A. Jacobs, and H. E. Hurlburt, Kuroshio Extention dynamics from satellite altimetry and a model simulation, *J. Geophys. Res*., vol.103, pp.8045–8057, 1996.

[23] K. Mizuno, and W. B. White, Annual and interannual variability in the Kuroshio current system, *J. Phys. Oceanogr*., vol.13, pp.1847–1867, 1983.

[24] T. Qu, H. Mitsudera, and B. Qiu, A climatological view of the Kuroshio/Oyashio system east of Japan, *J. Phys. Oceanogr*., vol.31, pp.2575–2589, 2001.

[25] E. R. Levine, and W. B. White, Bathymetric influences upon the character of North Pacific fronts, 1976–1980, *J. Geophys. Res*., vol.88, pp.9617–9625, 1983.

[26] P. P. Niiler, N. A. Maximenko, G. G. Panteleev, T. Yamagata, and D. B. Olson, Near-surface dynamical structure of the Kuroshio Extension, *J. Geophys. Res.*, vol.108, 3193, doi:10.1029/2002JC001461, 2003.

[27] N. Ebuchi, and K. Hanawa, Mesoscale eddies observed by TOLEX-ADCP and TOPEX/POSEIDON altimeter in the Kuroshio recirculation region south of Japan, *J. Oceanogr*., vol.56, pp.43–57, 2000.

[28] N. Ebuchi, and K. Hanawa, Trajectory of mesoscale eddies in the Kuroshio recirculation region, *J. Oceanogr*., vol.57, pp.471–480, 2001.

[29] H. Mitsudera, T. Waseda, Y. Yoshikawa, and B. Taguchi, Anticyclonic eddies and Kuroshio meander Formation, *Geophys. Res. Lett*., vol.28, pp.2025–2028, 2001.

[30] T. Kagimoto, and T. Yamagata, Seasonal transport variations of the Kuroshio: An OGCM simulation, *J. Phys. Oceanogr*., vol.27, pp.403–418, 1997.

[31] K. Akitomo, and M. Kurogi, Path transition of the Kuroshio due to mesoscale eddies: A two-layer, wind-driven experiment, *J. Oceanogr*., vol.57, pp.735–741, 2001.

[32] K. Ichikawa, Variation of the Kuroshio in the Tokara Strait induced by meso-scale eddies, *J. Oceanogr*., vol.57, pp.55–68, 2001.

[33] D. Zhang, T. N. Lee, W. E. Johns, C.-T. Liu, and R. Zantopp, The Kuroshio east of Taiwan: Modes of variability and relationship to interior ocean mesoscale eddies, *J. Phys. Oceanogr*., vol.31, pp.1054–1074, 2001.

[34] K. Wyrtki, and B. Kilonsky, Mean water and current structure during the Hawaii-to-Tahiti shuttle experiment,

J. Phys. Oceanogr., vol.14, pp.242–254, 1984.

[35] G. C. Johnson, B. M. Sloyan, W. S. Kessler, and K. E. McTaggart, Direct measurements of upper ocean currents and water properties across the tropical Pacific Ocean during the 1990's, *Prog. Oceanogr*., vol.52, pp.31–61, 2002.

[36] G. C. Johnson, M. J. McPhaden, G. D. Rowe, and K. E. McTaggart, Upper equatorial Pacific Ocean current and salinity variability during the 1996-1998 El Niño-La Niña cycle, *J. Geophys. Res*., vol.105, pp.1037–1053, 2000.

[37] G. C. Johnson, and D. W. Moore, The Pacific subsurface countercurrents and an inertial model, *J. Phys. Oceanogr*., vol.27, pp.2448–2459, 1997.

[38] G. Meyers, Variation of Indonesian throughflow and the El Niño - Southern Oscillation, *J. Geophys. Res.*, vol.101, pp.12,255–12,263, 1996.

[39] S. P. Murray, and D. Arrief, Throughflow into the Indian Ocean through the Lombok strait, January 1985-January 1986, *Nature*, vol.333, pp.444–447, 1988.

[40] Y. Masumoto, and T. Yamagata, Seasonal variations of the Indonesian throughflow in a general circulation model, *J. Geophys. Res.*, vol.101, pp.12,287–12,293, 1996.

[41] K. Wyrtki, An equatorial jet in the Indian Ocean, *Science*, vol.181, pp.262–264, 1973.

[42] J. J. O'Brien, and H. E. Hurlburt, Equatorial jet in Indian Ocean - Theory, *Science*, vol.184, pp.1075–1077, 1974.

[43] W. Han, J. P. McCreary Jr., D. L. T. Anderson, and A. J. Mariano, On the dynamics of the eastward surface jets in the equatorial Indian Ocean, *J. Phys. Oceanogr*., vol.29, pp.2191–2209, 1999.

[44] F. Schott, and J. P. McCreary Jr., The monsoon circulation of the Indian Ocean, *Prog. in Oceanogr.*, vol.51, pp.1–123, 2001.

[45] J. C. Swallow, R. L. Molinari, J. G. Bruce, O. B. Brown, and R. H. Evans, Development of near-surface flow pattern and water mass distribution in the Somali Basin in response to the southwest monsoon of 1979, *J. Phys. Oceanogr*., vol.13, pp.1398–1415, 1983.

[46] J. G. Bruce, M. Fieux, and J. Gonella, A note on the continuance of the Somali eddy after the cessation of the Southwest Monsoon, *Oceanology Acta*, vol.4, pp.7–9, 1981.

[47] A. Wirth, J. Willebrand, and F. Schott, Variability of the Great Whirl from observations and models, *Deep Sea Res. II*, vol.49, pp.1279–1295, 2002.

[48] J. R. E. Lutjeharms, The exchange of water bewteen the South Indian and South Atlantic Oceans, *The South Atlantic: Present and past circulation*, G. Wefer, W. H. Berger, G. Siedler and D. Webb (eds.), pp.122–162, Springer-Verlag, Berlin-Heidelberg, Germany, 1996.

[49] J. R. E. Lutjeharms, and R. C. van Ballegooyen, The retroflection of the Agulhas Current, *J. Phys. Oceanogr*., vol.18, pp.1570–1583, 1988.

[50] T. Whitworth, III and R. G. Peterson, Volume Transport of the Antarctic Circumpolar Current from Bottom Pressure Measurements, *J. Phys. Oceanogr*., vol.15, pp.810–816, 1985.

[51] S. T. Gille, Mean sea surface height of the Antarctic Circumpolar Current from Geosat data: Method and application, *J. Geophys. Res*., vol.99, pp.18, 255–18, 273, 1994.

[52] C. W. Hughes, and E. R. Ash, Eddy forcing of mean flow in the Southern Ocean, *J. Geophys. Res*., vol.106, pp.2713–2722, 2001.

[53] A. H. Orsi, T. Whitworth III, and W. D. Nowlin Jr, On the meridional extent and fronts of the Antarctic Circumpolar Current, *Deep Sea Res. I*, vol.42, pp.641–673, 1995.

[54] S. S. Jacobs, On the nature and significance of the Antarctic Slope Front, *Marine Chemistry*, vol.35, pp.9–24, 1991.

[55] A. M. Paiva, J. T. Hargrove, E. P. Chassignet, and R. Bleck, Turbulent behavior of a fine mesh (1/12) numerical simulation of the North Atlantic, *J. Mar. Sys*., vol.21, pp.307–320, 1999.

[56] X. Guo, H. Hukuda, Y. Miyazawa, and T. Yamagata, A triply nested ocean model for simulating the Kuroshio - Roles of horizontal resolution on JEBAR, *J. Phys. Oceanogr*., vol.33, pp.146–169, 2003.

[57] W. Ohfuchi, H. Nakamura, M. K. Yoshioka, T. Enomoto, K. Takaya, X. Peng, S. Yamane, T. Nishimura, Y. Kurihara, and K Ninomiya, 10-km Mesh Meso-scale Resolving Simulations of the Global Atmosphere on the Earth Simulator – Preliminary Outcomes of AFES (AGCM for the Earth Simulator). *J. Earth Sim.*, (this issue).